ACS APPLIED MATERIALS & INTERFACES

Tuning the Nonlinear Optical Properties of MoS_2 by Interfacing with Bay- or Imide-Substituted Perylene Diimides

Eleni Nikoli,○ Ruben Canton-Vitoria,○ Georgios Skentzos,○ Efrosyni Pramatioti,○ Nathalie Zink-Lorre, Ana Maria Gutiérrez-Vílchez, Fernando Fernández-Lázaro,* Raul Arenal,* Stelios Couris,* and Nikos Tagmatarchis*

Cite This: https://doi.org/10.1021/acsami.5c25463

Read Online

ACCESS | Metrics & More | Article Recommendations | Supporting Information

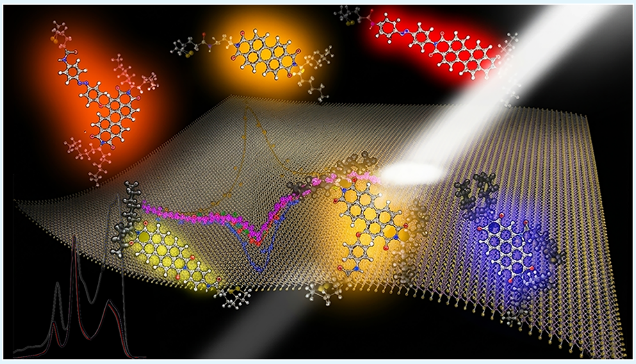

ABSTRACT: We have investigated the tuning of nonlinear optical (NLO) properties in semiconducting MoS_2 nanosheets through covalent functionalization with bay- or imide-substituted perylene diimide (PDI) derivatives. Five MoS_2–PDI hybrid nanomaterials **1a**–**5a** were synthesized by attaching PDI variants featuring azobenzene or other substituents, characterized via Raman, IR, TGA, STEM-EDS, ultraviolet–visible (UV–vis), photoluminescence, and electrochemical analyses, and evaluated for NLO response under nanosecond (4 ns, 1064/532 nm) and femtosecond (70 fs, 800/400 nm) laser excitations. The hybrids exhibit enhanced and tunable NLO-absorptive (switching from saturable to reverse-saturable absorption with intensity) and NLO-refractive (self-focusing) responses compared to exfoliated MoS_2, with **1a** and **2a** (azobenzene-substituted PDIs) showing the strongest effects due to efficient electron-transfer and -resonant excitations. Hybrids demonstrate superior NLO susceptibility (χ^3) values, particularly under resonant 532 nm excitation, with $\mathrm{Im}\{\chi^3\}$ values of up to $-514.7 \pm 57.4 \times 10^{-13}$ esu·mL/mg for **2a** at low intensities, attributed to Pauli blocking, defect states, and two-photon processes. Hybrids having bay-substituted PDIs grafted on MoS_2 enhance conjugation and performance over imide variants, enabling applications in optical-limiting, mode-locking, and photonic devices. Threshold intensities for NLA switching (150–250 MW/cm^2) exceed those of MoS_2, highlighting the stability for high-power uses. The developed hybrid materials advance two-dimensional transition-metal dichalcogenide-based optoelectronics by overcoming light–matter interaction limits through molecular antenna effects from PDIs. The study underscores the substituent position and azobenzene integration as levers for NLO optimization in hybrid nanoarchitectures.

KEYWORDS: *transition-metal dichalcogenides, molybdenum disulfide, perylene diimide, functionalization, nonlinear optics*

■ INTRODUCTION

Transition-metal dichalcogenides (TMDs) constitute a rapidly emerging family of two-dimensional (2D) layered nanomaterials that have demonstrated unprecedented prospects in a wide range of applications, with the optoelectronic ones being among the most popular.[1] TMDs' excellence in photonic applications is largely attributed to their unique band structure and tunable bandgap, which is thickness-dependent and evolves from an indirect bandgap semiconductor for bulk materials to a direct bandgap semiconductor scaled down to a single layer, due to the reduced dielectric screen effect.[2] Particularly, the tunable bandgap renders distinct characteristics to TMDs, such as significant carrier mobility and an outstanding nonlinear absorptive (NLA) response.[2] As a result of the robust optical nonlinearity and swift response as well as broad optical absorption, high damage threshold, and excellent chemical stability of 2D TMDs, nonlinear optical (NLO) processes have been studied toward the fabrication of on-chip photonic and optoelectronic devices. Optical switching,[3] optical frequency conversion,[4] significant optical-limiting efficiency,[5−7] exceptional broadband saturable absorption (SA)[8,9] and size-dependent NLO response[5] are among the NLO processes studied. The NLO properties of TMDs are dependent on inherent structural characteristics, such as the phase, symmetry, crystal orientation, number of layers, and defects.[10] Tuning of these factors enables the modulation of the NLO properties of TMDs, which can also be influenced by excitonic effects. In fact, as evidenced by our recent study on

Received: December 17, 2025
Revised: January 30, 2026
Accepted: February 1, 2026

ACS Publications

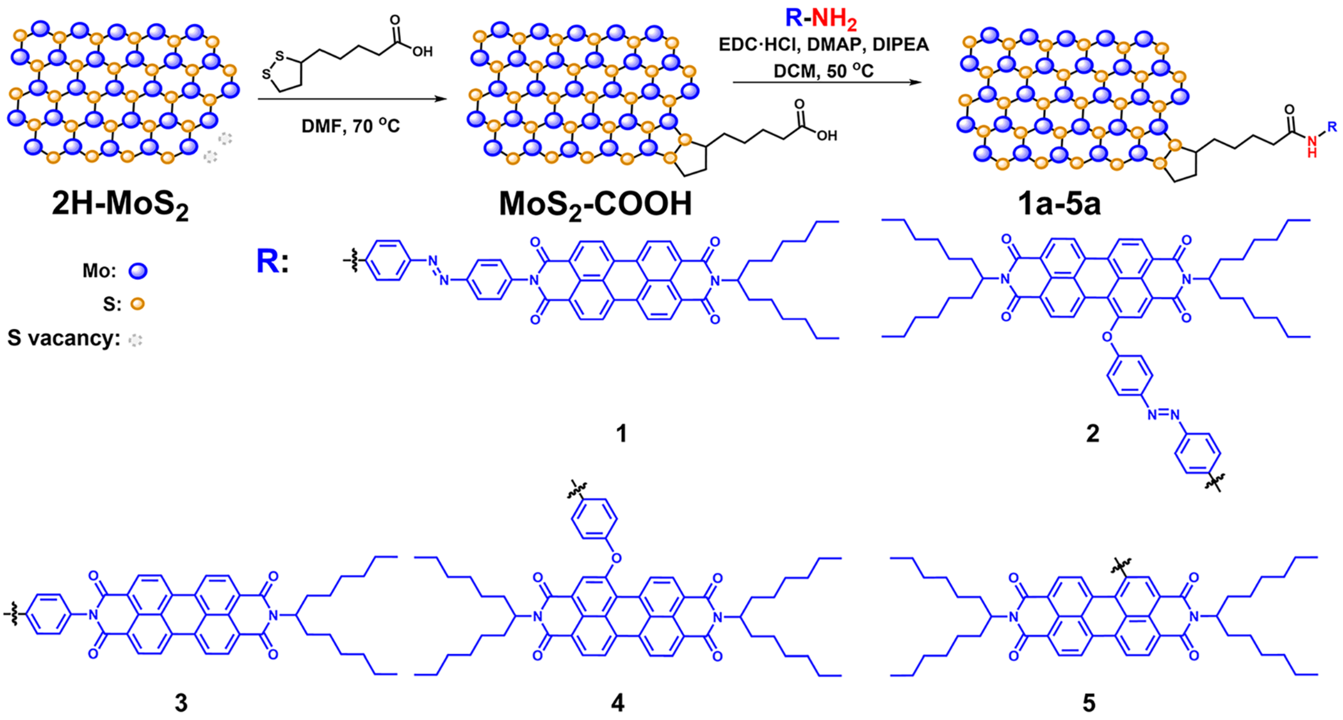

Figure 1. Illustrative preparation of MoS_2−PDI hybrid materials **1a**−**5a**.

both MoS_2 and WS_2, as representatives of the TMD family, by controlling the crystalline phase of the nanosheets, that is, their semiconducting or metallic character, their NLO response can be greatly modulated.[11] However, the layered nature of TMDs restricts the light−matter interaction within the material, and therefore the need to enhance this interaction still remains, in line with the intense research interest toward more efficient optoelectronic devices. A plausible solution to this challenge lies in the chemical functionalization of 2D TMD nanosheets that allows the incorporation of electron acceptor and/or donor species conjugated on the surface of the nanosheets to serve as antennas, to improve polarization induced on hybrids, while allowing control over the electronic band structure within the material.[12]

Excellent candidates to fulfill such an endeavor are rigid organic compounds with delocalized π-conjugated systems, showing high charge transfer and optical performances. Perylene diimide (PDI) derivatives represent such a versatile family of dyes, renowned for their synthetic adaptability and easily modifiable electronic character.[13] Indeed, these derivatives have emerged as highly promising molecular materials in organic optoelectronic applications, owing to their tunability and exceptional photophysical properties.[14−17] A plethora of PDI derivatives have been deployed for electronic and light-harvesting applications owing to their exceptional stability, strong fluorescence, and broad absorption.[18] Their large two-photon absorption (2A) cross section[19] also makes them ideal and excellent NLO materials.[20,21]

Conversely, azobenzenes, belonging to the wider class of diazenes, are π-conjugated compounds composed of two phenyl rings linked by a nitrogen−nitrogen double bond (N═N), with easily, precisely, and facilely adjusted properties via derivatization and incorporation of various functional groups at the phenyl rings.[22] For example, different substituents at the phenyl ring of azobenzenes alter the absorption profile, which can be shifted from the UV−vis region to the NIR region of the electromagnetic spectrum. The incorporation of electron-donating amine groups at the *para*-position of the phenyl ring, such as, for example, in azoanilines, red-shifts the absorption in comparison with the unsubstituted azobenzene, while, on the other hand, extension of the π-conjugation skeleton enhances the 2A properties.[23] Notably, azobenzenes have been employed as ligands for chromophores, such as triarylamine[24] and pyrene,[25] among others,[26] enabling the tuning of NLO properties. Markedly, bay substitution of PDI with azobenzene resulted in a larger NLO response compared to imide-substituted PDI, as supported by experimental and theoretical calculations and attributed to the modification of the electronic character of the PDI upon derivatization with azobenzene.[27]

With the aforementioned in mind and the rich chemistry of PDIs that enables their seamless combination with target components, incorporation of azobenzenes into the structure of PDIs is of great and significant importance. While the NLO performance of perylene derivatives has been well documented[28−32] and might complement the properties of MoS_2 within the realization of the corresponding hybrid materials, an investigation that remains to be unraveled concerns the integration of azobenzenes into those two-dimensional hybrid nanoarchitectures. Herein, having established the chemistry of functionalization of a PDI derivative on semiconducting MoS_2 nanosheets via covalent bonding,[33] we present the preparation, characterization, and NLO assessment of five new MoS_2-based hybrid materials featuring different PDI derivatives covalently anchored on the MoS_2 framework. The simultaneous tailoring of properties of both PDIs and MoS_2 is achieved within the formation of the nanohybrids, where π−π stacking is mitigated for PDIs, while substituents are inserted at defined bay and imide positions, introducing another dimension in both materials' 2D structure and molecule's planar conformation, respectively. Full spectroscopic and thermal and electron microscopy imaging characterization is accompanied by a detailed NLO investigation assessment of all new nanohybrids.

https://doi.org/10.1021/acsami.5c25463

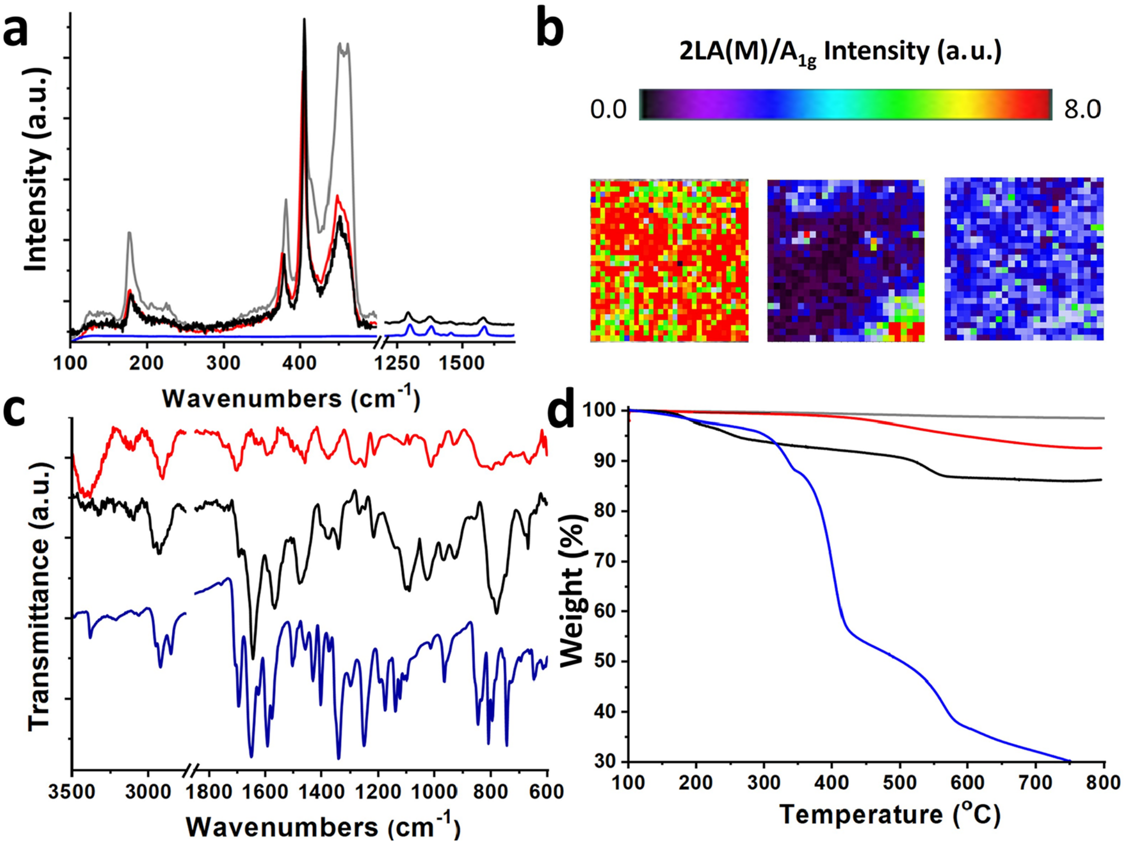

Figure 2. (a) Raman spectra (633 nm) of PDI derivative **1** (blue), exfoliated MoS_2 (gray), MoS_2−COOH (red), and MoS_2−PDI hybrid material **1a** (black). (b) Raman spectral maps of the 2LA(M)/A_{1g} ratio for exfoliated MoS_2 (left), MoS_2−COOH (center), and MoS_2−PDI hybrid material **1a** (right). (c) IR spectra and (d) TGA graphs of PDI derivative **1** (blue), MoS_2−COOH (red), and MoS_2−PDI hybrid material **1a** (black).

The results indicate the development of new NLO 2D nanomaterials that have potential pivotal applications in optical devices and signal conversion.

RESULTS AND DISCUSSION

The synthesis of PDI derivatives **1**−**5** was conducted following literature procedures.[27,34−36] The substituents on the imide position are electronically decoupled from the PDI core due to the presence of nodes at the imide nitrogen atoms in the Highest Occupied Molecular Orbital (HOMO) and Lowest Unoccupied Molecular Orbital (LUMO), hence PDI derivative **1** is considered upon derivatization at the imide position as composed of two independent subunits: the PDI core and the amine-rich azobenzene (Figure 1). Conversely, functionalization of PDI at the bay position with azobenzene species enhances aromatic conjugation in PDI derivative **2**. Furthermore, other moieties have been employed as reference compounds in this study, which can be classified into two groups: those with an electronically decoupled substituent (imide substitution, e.g., **3**) and those with a conjugated substituent (bay substitution, e.g., **4** and **5**). Consequently, the overall effects on the NLO properties of perylene and azobenzene on MoS_2 can be effectively differentiated, based on (a) the type of electron-donating groups, (b) the degree of aromatic conjugation, and (c) the PDI functionalization position (Figure 1).

Semiconducting MoS_2 was exfoliated with chlorosulfonic acid[37] and premodified with lipoic acid via filling of the MoS_2 edges' sulfur vacancies with the sulfur atoms of 1,2-dithiolane,[38] to incorporate carboxylic acid species at the periphery of the nanosheets, yielding modified MoS_2−COOH. Next, condensation of the free −COOH units with PDI derivatives **1**−**5** furnished MoS_2−PDI hybrids **1a**−**5a**, as shown in Figure 1.

Raman spectroscopy serves as a frontline technique for the characterization of modified MoS_2 nanomaterials. Specifically, upon 633 nm excitation, exfoliated MoS_2 exhibits three characteristic bands, namely, $E_{2g}{}^1$, and A_{1g}, corresponding to in-plane and out-of-plane vibrations at 381 cm^{-1} and 407 cm^{-1}, respectively, and defect-induced 2LA(M), at 456 cm^{-1}. Focusing on monitoring Raman spectral alterations of MoS_2−PDI hybrid materials **1a**−**5a**, in comparison to exfoliated MoS_2 and MoS_2−COOH, a decrease of the intensity ratio 2LA(M)/A_{1g}, from 7.5 for exfoliated MoS_2 to 3.4 for MoS_2−COOH, is observed, indicating the sulfur-vacancy restoration by the sulfur atoms of the 1,2-dithiolane derivative. Simultaneously, after conjugation of the five different PDIs in MoS_2 within hybrids **1a**−**5a**, no appreciable variation in the spectral Raman features is detected (Figures 2a and S1), suggesting that the condensation reaction between PDI derivatives **1**−**5** and MoS_2−COOH does not affect the lattice of MoS_2. Additionally, Raman spectral modes related to PDI derivatives **1**−**5**, at 1289, 1375, and 1582 cm^{-1}, corresponding to C═C aromatic and imide vibrations, confirm their presence in MoS_2−PDI hybrid materials **1a**−**5a**. Additionally, Raman spectral mapping on a 35 × 35 μm^2 area also confirms the decrement of the relative intensity of the 2LA(M)/A_{1g} ratio in MoS_2−COOH and **1a**−**5a** hybrids, in comparison with exfoliated MoS_2 (Figures 2b and S2).

https://doi.org/10.1021/acsami.5c25463
ACS Appl. Mater. Interfaces XXXX, XXX, XXX−XXX

The structures of MoS_2−PDI hybrid materials **1a**−**5a** were further monitored by IR spectroscopy. The IR spectrum of MoS_2−COOH is distinctly characterized by carbonyl and O−H stretching vibrations of −COOH at 1698 cm^{-1} and 3600−3200 cm^{-1}, respectively, and C−H vibrations at 2900 cm^{-1}. Conversely, PDI derivatives **1**−**5** exhibit rich characteristic features. Regarding **1**, the bands due to the symmetric and antisymmetric stretching modes of the carbonyl imides are evident at 1696 and 1651 cm^{-1}, as well as the conjugated C=C stretching modes at 1574 cm^{-1} (Figure 2c). The aforementioned PDI's signature bands are prominently evident for all **1a**−**5a** hybrids, in comparison to MoS_2−COOH signatures in IR spectroscopy. More specifically, the IR spectrum of MoS_2−PDI hybrid materials **1a**−**5a** is characterized by an enhancement in the carbonyl imide features at 1694 and 1645 cm^{-1}, while the −COOH signature bands are remarkably diminished. Such change confirms the success of the condensation reaction between **1** and MoS_2−COOH. This information aligns closely with our previous results,[33] and similar reasoning applies to the rest of the MoS_2−PDI hybrid materials **2a**−**5a**, as depicted in Figure S3.

Thermogravimetric analysis (TGA) offers a quantitative assessment of the loading of PDI in **1a**−**5a**. Exfoliated MoS_2 demonstrates thermal stability in the temperature range of 100−800 °C, under inert conditions, affirming the high quality of the exfoliated nanosheets. On the other hand, the MoS_2−COOH thermogravimetric curve shows 2.6% weight loss up to 500 °C, due to thermal decomposition of the organic addend. After the subsequent addition of PDI derivatives **1**−**5**, the percentage weight loss of MoS_2−PDI hybrid materials **1a**−**5a** amplifies to 5−8% (Figures 2d and S4). These values correspond to the functionalization degree of approximately 1 PDI unit per 60 MoS_2 units in **1a**−**5a** with minor fluctuations among the different hybrids.

Scanning transmission electron microscopy (STEM) is a powerful technique for acquiring critical local-scale insights into the structural and chemical compositions of complex materials at subnanometer and atomic resolutions. Atomic-resolution structural and chemical characterization were performed by using local-scale STEM. STEM analysis of the MoS_2−PDI hybrid material **4a** is detailed in Figure 3. Data for the other MoS_2−PDI hybrid materials **1a**, **2a**, **3a**, and **5a** are provided in Figure S5. Briefly, Figure 3a presents a low-magnification High-Angle Annular Dark-Field (HAADF)-STEM image of the MoS_2−PDI hybrid material **4a** flakes. Figure 3b shows a higher-magnification HAADF-STEM image in which bright, small domains are clearly visible. To determine the composition of these bright domains, energy-dispersive X-ray spectroscopy (EDS) analysis was performed within the red marked region of Figure 3b. The resulting EDS spectrum (Figure 3c) confirms the presence of C−K and O−K signals, corroborating that these bright domains correspond to the perylene-functionalized moieties.

The optical analysis of MoS_2−PDI hybrid materials **1a**−**5a** started with electronic absorption (UV−vis) spectroscopy. The absorption profiles of MoS_2 nanosheets typically show four characteristic bands. The bands at 410 and 477 nm are attributed to excitonic transitions between higher-density states in the valence and conduction bands (M point of the Brillouin zone).[39−41] Additionally, the bands at 620 and 683 nm correspond to A- and B-excitons, arising from direct transitions at the K point. Their energy difference, i.e., ~60 nm (~0.20 eV), is indicative of the strength of the spin−orbit interaction. The aforementioned characteristic bands of 2H-MoS_2 overlap with the signature bands of perylene. On the other hand, the continuous absorption between 300 and 400 nm, which is abnormal in intact MoS_2, might be associated with the presence of an azobenzene unit, as seen in MoS_2−PDI hybrid materials **1a** and **2a** (Figures 4a and S6a, respectively). Based on the absorptivity of each species, the contribution of perylene is expected to be approximately 1% of that of MoS_2; however, due to the electronic interaction between both species, the NLO response can be fully transferred. Additionally, the absorption bands due to PDIs were clearly unveiled after subtracting those of MoS_2, revealing the broadened but not shifted PDI bands (inset to Figure 4a, for MoS_2−PDI hybrid material **1a**, and inset to Figure S6 for MoS_2−PDI hybrid materials **2a**−**5a**). The PDI derivative **1a** exhibits a broad absorption band centered at 373 nm, associated with the azobenzene moiety incorporated at the imide position, in addition to the characteristic PDI bands centered at 457, 489, and 525 nm, which are attributed to the S_0−S_1 electronic transitions in the 0−2, 0−1, and 0−0 vibronic states.[27,42,43] Similarly, hybrid material **2a** displays absorption maxima at 382, 460, 495, and 530 nm (Figure S6a). These spectral distinctions, when comparing **1a** and **2a**, stem from the differing electronic influences of imide versus bay substitution within the PDI framework. Amine substitution in PDI derivatives results in absorption bands centered at 457, 488, and 525 nm for hybrid material **3a**, and at 480, 510, and 547 nm for hybrid material **4a**, consistent with the trend observed for hybrid materials **1a** and **2a**, where bay substitution leads to lower-energy absorption (Figure S6b,c). Hybrid material **5a** exhibits a broad absorption centered at 419 nm with shoulders at 387 and 403 nm, along with a broad, structureless band at 568 nm (Figure S6d).

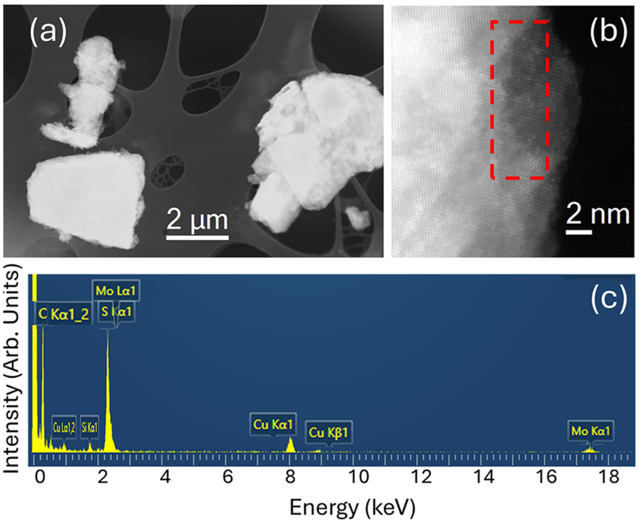

Figure 3. STEM-HAADF imaging and STEM-EDS analyses of the MoS_2−PDI hybrid material **4a**. (a) and (b) STEM-HAADF low-magnification and HRSTEM images of these flakes. (c) EDS sum of spectra recorded in the red highlighted rectangular region of **4a** based on the flakes in (b).

Furthermore, photoluminescence emission spectroscopy provides additional insights, particularly into electronic interactions between MoS_2 and PDIs in the excited state. The emission spectrum of PDI derivative **1** (excitation at 440 nm) shows two dominant bands at 532 and 573 nm (Figure 4b). In parallel, PDI derivative **2** displays emission bands at

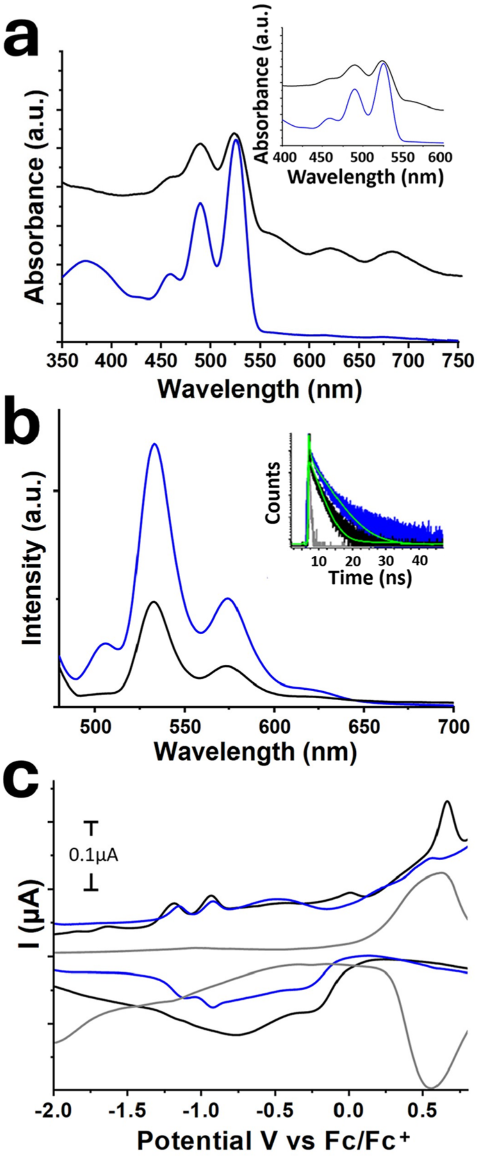

Figure 4. (a) UV−vis spectra of PDI derivative **1** (blue) and MoS_2−PDI hybrid material **1a** (black), obtained in dichloromethane. Inset: UV−vis spectrum of MoS_2−PDI hybrid material **1a**, after subtraction of absorption due to MoS_2 (black), in comparison with the same optical concentration spectrum of PDI derivative **1** (blue). (b) Emission spectra (excitation at 440 nm) of PDI derivative **1** (blue) and MoS_2−PDI hybrid material **1a** (black), obtained under equal optical absorbance at the excitation wavelength in dichloromethane. Inset: Emission decay of PDI derivative **1** (blue), MoS_2−PDI hybrid material **1a** (black), and the corresponding fitting (green). (c) Square-wave pulse voltammetry graphs of exfoliated MoS_2 (gray), PDI derivative **1** (blue), and MoS_2−PDI hybrid material **1a** (black) in dry DMF, with 0.1 M tetrabutylammonium hexafluorophosphate as the electrolyte.

557 and 595 nm, indicating that the substitution at the bay position results in the existence of lower-excited-state energy levels, contrary to PDI derivative **1**, following the same pattern as in the UV−vis absorption spectrum (Figure S7a). Similar phenomena are evident in PDI derivatives **3** and **4**, with the former exhibiting two emission bands centered at 533 and 574 nm and the latter at 555 and 590 nm (Figure S7b,c), where once again the emission energy is lower in the case of the bay-substituted PDI derivative **4**. On the other hand, PDI derivative **5** shows a different emission profile, characterized by two emission bands at 477 and 512 nm, and a broad one centered at 663 nm (Figure S7d). Focusing on MoS_2−PDI hybrid materials **1a**−**4a**, a strong emission quenching effect was consistently recorded across all hybrids, under equal optical absorbance at the excitation wavelength. It should be pointed out that the emission bands of bay-substituted MoS_2−PDI hybrid materials in **2a** and **4a** were blue-shifted for 13 and 5 nm, respectively, compared to the emission band of the corresponding PDI derivatives **2** and **4**. Interestingly, the broad emission band of PDI derivative **5** at 663 nm does not appear in MoS_2−PDI hybrid material **5a** (Figures 4b for **1a** and S7 for **2a**−**5a**). On the contrary, no shift is observed for the emission bands of hybrids **1a** and **3a**. The aforementioned changes in emission profiles have been previously observed in the literature and possibly indicate electron and/or energy transfer from MoS_2 to PDI concerning the bay-substituted hybrids.[33]

Next, the emission decay was assessed by performing lifetime analysis with the time-correlated single-photon counting (TCSPC) method. PDI derivatives **1**−**5** exhibit a monoexponential emission decay, with values ranging between 2.00 and 5.00 ns. On the other hand, MoS_2−PDI hybrid materials **1a**−**5a** show a reduction in lifetime due to the presence of a second component, which is around 10 times faster. For example, PDI derivative **1** (inset of Figure 4b) shows a lifetime of 2.35 ns, while in MoS_2−PDI hybrid material **1a**, the second component has a lifetime of 270 ps. Overall, steady-state and time-resolved fluorescence emission and decay align with the existence of a new relaxation path, corresponding to a new electron−hole transfer process, in agreement with previous studies.[33]

Next, electrochemical assays employing differential pulse voltammetry (DPV) were performed in dry *N*,*N*-dimethylformamide (DMF) under a nitrogen atmosphere, with 0.1 M tetrabutylammonium hexafluorophosphate as the electrolyte. Platinum served as the reference and auxiliary electrodes, and glassy carbon served as the working electrode. First, the impact of azobenzene substitution at the imide position within PDI derivative **1** produces reversible reduction peaks at −0.91 and −1.11 V, with an oxidation peak recorded at 0.55 V (Figure 4c). When the azobenzene derivatization of PDI is at the bay position in PDI derivative **2**, the reduction peaks shift to −0.93 and −1.18 V, with an oxidation peak at 0.51 V (Figure S8a). The effect of PDI substitution with an aniline moiety is also interesting, yielding reduction potentials for **3** at −0.93 and −1.23 V and for **4** at −0.95 and −1.27 V (Figure S8b,c). Finally, PDI derivative **5** is characterized by the presence of reduction potentials at −1.13 and −1.41 V, and oxidation potentials at −0.05 and +0.44 V (Figure S8d). On the other hand, exfoliated MoS_2 exhibits a reduction peak at −1.21 V and two characteristic oxidation potentials at 0.38 and 0.58 V (Figure 4c). The first oxidation can be attributed to the oxidation of Mo species, primarily arising from defects at the edges, whereas the one at 0.58 V corresponds to the valence band.[44−46] Interpretation of the redox data for MoS_2−PDI hybrid materials **1a**−**5a** becomes more complex due to the broadening of the signals and superposition of the redox peaks. The edge oxidation peak of MoS_2 at 0.38 V is reduced and becomes even invisible in some of the hybrid materials, as shown for **1a** in Figure 4c. This decrement of the first oxidation signal is directly associated with covalent functionalization as the 1,2-dithiolane addition of lipoic acid in MoS_2−COOH passivates and protects the edges of the nanosheets

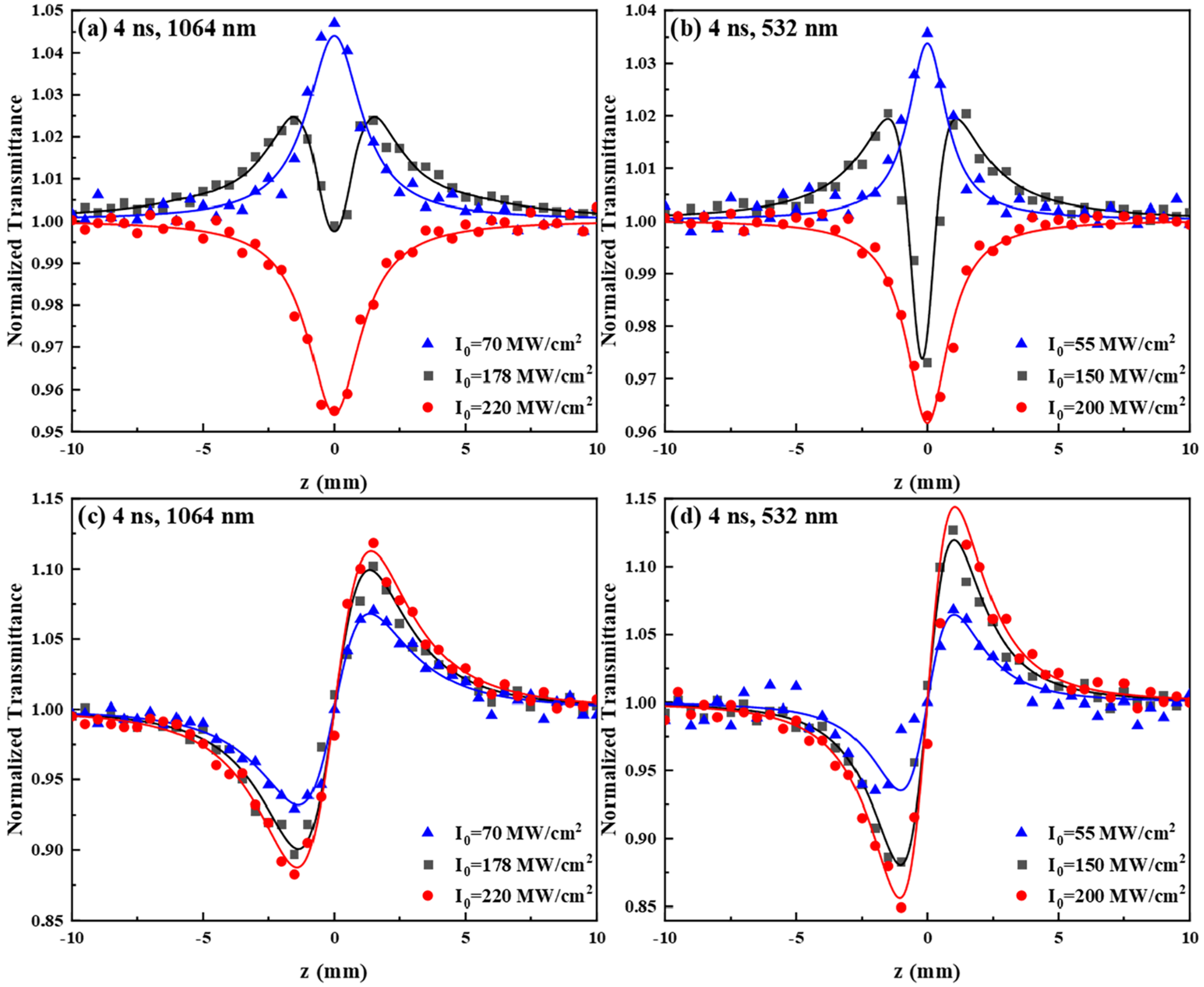

Figure 5. (a, b) OA and (c, d) “divided” Z-scans of MoS_2−PDI hybrid material **3a** in DMF (0.1 mg/mL) obtained under 1064 and 532 nm excitation, using different laser intensities.

against oxidation. The reduction and oxidation potentials of PDI derivatives within hybrids **1a**−**5a** are also affected. For example, the reduction potentials of **1** versus **1a** shift from −0.91 and −1.11 V to −1.05 and −1.18 V (Figure 4c), respectively, and those for **2** versus **2a** shift from −0.93 and −1.18 V to −1.01 and −1.26 V (Figure S8a), respectively. On the other hand, the oxidation potentials for PDI derivatives **1** and **2** versus MoS_2−PDI hybrid materials **1a** and **2a** practically remain unaltered. Similar shifts are observed in MoS_2−PDI hybrid materials **3a**−**5a** (Figure S8b−d). Next, Figure S9 shows the electronic states of MoS_2 and hybrid materials **1a**−**5a**. Specifically, the electronic structures of MoS_2 and the LUMO levels of the perylene derivatives were converted to a vacuum-energy diagram referenced to the ferrocene/ferrocenium (Fc/Fc^+) redox couple, whereas the deep HOMO levels of the perylenes were estimated by adding the lowest-energy PL transition. Materials **1a** and **2a** exhibit a type-II band alignment, in which the HOMO levels (−5.91 and − 5.87 eV, respectively) lie deeper than the valence-band maximum of MoS_2 at −5.38 eV. Consequently, under light irradiation, photogenerated holes in the perylene units can be transferred to MoS_2, in agreement with previous reports.[33,46] A similar analysis can be applied to materials **3a**−**5a**. Additionally, the PDI substitution pattern (bay versus imide) plays a critical role. Bay substitution generally induces a twisted perylene core and modifies the HOMO−LUMO energy levels compared with planar imide-substituted derivatives. These structural and electronic differences affect the surface interactions between the perylene units and MoS_2, thereby modulating the efficiency of photoinduced electron and/or energy transfer. Nevertheless, in all hybrid systems, the perylene and MoS_2 components remain in intimate electronic contact, enabling the NLO response to extend throughout the entire material.

NLO Response of MoS_2−PDI Hybrid Materials 1a−5a

The NLO-absorptive (NLA) and -refractive (NLR) responses of the MoS_2−PDI hybrid materials **1a**−**5a** and exfoliated MoS_2 were studied under nanosecond and femtosecond laser-excitation conditions, employing 4 ns, 1064 and 532 nm, and 70 fs, 800 and 400 nm laser pulses. It is important to note that the excitation at 1064 and 800 nm corresponds to nonresonant excitation conditions, while the excitation at 532 and 400 nm corresponds to resonant excitation (see, e.g., the UV−vis absorption spectra of **1a**−**5a** in Figures 4a and S7a).

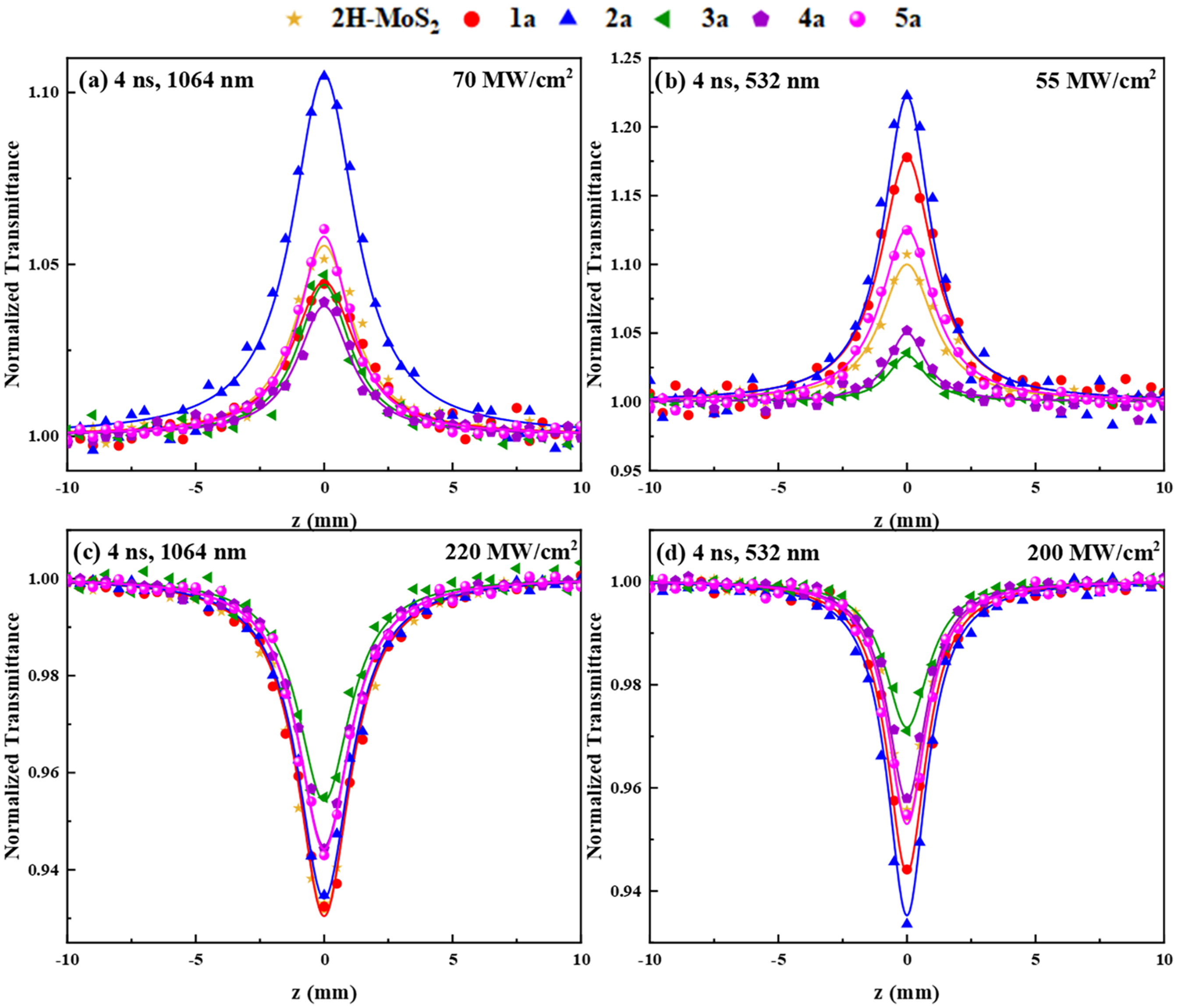

Figure 6. OA Z-scans of MoS$_2$−PDI hybrid materials **1a**−**5a** in DMF (0.1 mg/mL), under 4 ns, 1064 and 532 nm laser excitation, using low (a, b) and high (c, d) laser intensities.

The use of resonant and nonresonant excitations allows for the assessment of any enhancement of the NLO response due to resonant states of the studied materials. The key findings concerning the NLO response of MoS$_2$−PDI hybrid materials **1a**−**5a** are presented in the following. For completeness and comparison purposes, the exfoliated MoS$_2$ was also studied under identical experimental conditions to those used for the MoS$_2$−PDI hybrid materials **1a**−**5a**.

NLO Response under 4 ns, 1064/532 nm Laser Excitation

In a recent work,[11] investigating among other things, the NLO response of MoS$_2$ under 4 ns, 1064 and 532 nm laser-excitation conditions, it was reported that at both excitation wavelengths, MoS$_2$ exhibits saturable absorption (SA) (i.e., negative nonlinear absorption coefficient β, β<0, $\mathrm{Im}\chi^{(3)} < 0$) under low-laser intensity excitation, while at higher-laser intensities, its NLA response changes to reverse-saturable absorption (RSA) (i.e., positive nonlinear absorption coefficient β, β>0, $\mathrm{Im}\chi^{(3)}$ >0). As far as the NLR response is concerned, it remains unaltered, i.e., self-focusing (i.e., γ'>0; $\mathrm{Re}\chi^{(3)}$ >0), in both cases. In the present study, aiming to investigate the NLO response of some MoS$_2$−PDI hybrid materials, i.e., **1a**−**5a**, some exfoliated MoS$_2$ dispersions were measured again, under experimental conditions identical with those used for the hybrid materials, for comparison reasons. The Z-scan measurements, performed on different-concentration dispersions of exfoliated MoS$_2$ in DMF, have fully confirmed the findings of ref 11. So, the NLA response of exfoliated MoS$_2$ dispersions, under 1064 nm excitation, was found to change from SA to RSA for intensities higher than ∼100 MW/cm^2; a similar situation was confirmed for the case of 532 nm excitation, for intensities higher than ∼60 MW/cm^2.

The MoS$_2$−PDI hybrid materials **1a**−**5a** were found to follow a similar behavior. As an example, in Figure 5a,b, some representative Open-Aperture (OA) Z-scans of **3a** are presented, obtained at different incident laser intensities in the range of 50−220 MW/cm^2. As is shown, at low intensities, they all exhibited a transmittance maximum, i.e., SA, while at higher intensities, a dip is gradually formed. At even higher intensities, a transmittance minimum, i.e., RSA is clearly established. The corresponding “divided” Z-scans, depicted in

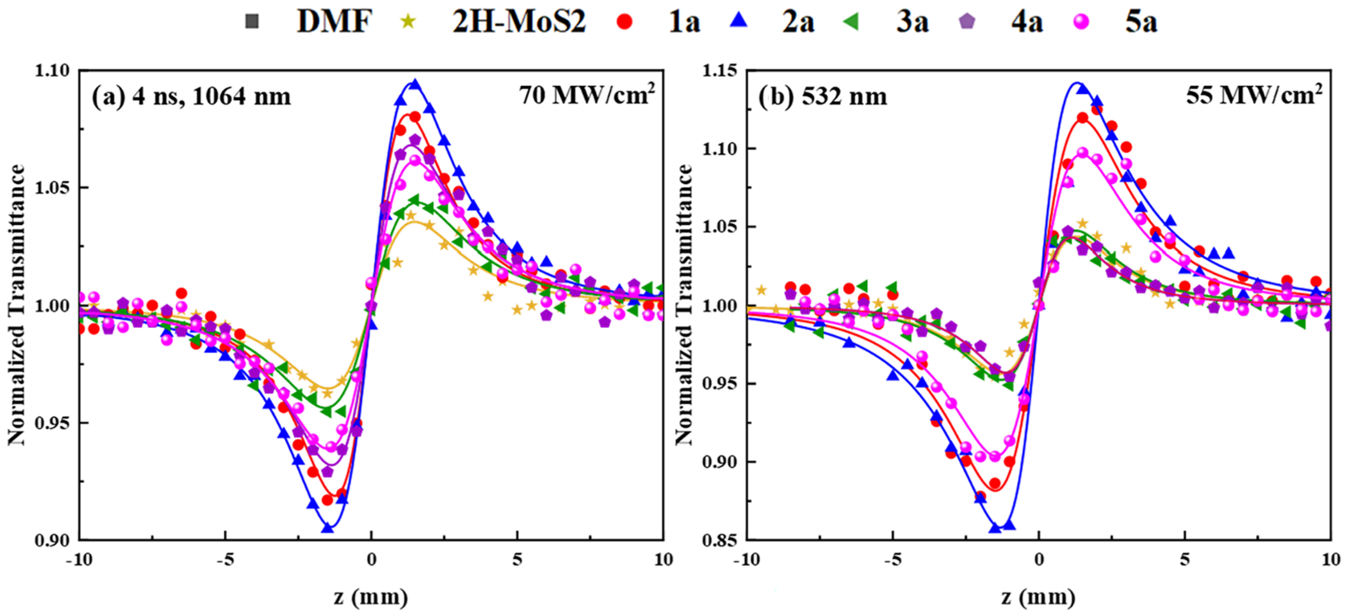

Figure 7. "Divided" Z-scans of MoS_2−PDI hybrid materials **1a**−**5a** in DMF (0.1 mg/mL) under 4 ns (a) 1064 and (b) 532 nm laser excitation.

Figure 5c,d, exhibit a valley−peak transmittance configuration, i.e., self-focusing for both low- and high-laser intensities. In addition, as can also be seen in Figure 5, the difference between the valley and the peak of the normalized transmission of the "divided" Z-scans (often denoted as $\Delta T_{v\text{-}p}$) was found to increase with the laser intensity. The same behavior was confirmed for the MoS_2−PDI hybrid materials **2a**−**5a** as well.

For the more detailed investigation of the NLO response of the MoS_2−PDI hybrid materials **1a**−**5a**, several different-concentration dispersions were prepared, i.e., 0.06−0.39 mg/mL, and studied under 532 and 1064 nm excitation by the Z-scan technique. The measurements were performed using both low- and high-laser intensities. So, first, in Figure 6a,b, some representative OA Z-scans of **1a**−**5a** and MoS_2 dispersions in DMF (0.1 mg/mL) are presented, obtained using relatively low intensity, i.e., 70 MW/cm^2 at 1064 nm, and 55 MW/cm^2 at 532 nm. The solid symbols correspond to the experimental data points, while the continuous lines correspond to the fitting of the experimental data points by eq (S1). As is shown, all dispersions exhibited SA behavior, while the neat solvent, i.e., DMF, exhibited negligible NLO response (both absorption and refraction) for the range of laser intensities employed. Therefore, the OA Z-scans directly reveal the nonlinear absorption of **1a**−**5a**. From the comparison of the magnitude of the transmittance maxima of these OA Z-scans, it becomes evident that **1a**−**5a** exhibit stronger SA response under 532 nm excitation, attributed to the resonant excitation at this wavelength. In addition, **2a**, **1a**, and **5a** exhibited stronger SA (in decreasing order) than MoS_2, while **4a** and **3a** presented lower SA. In the case of 1064 nm excitation, **2a** exhibited again the strongest SA, followed by **5a**, both having a stronger response than MoS_2. **1a** and **3a** exhibited similar-magnitude SA and lower than that of MoS_2; hybrid **4a** exhibited the lowest SA.

Concerning the NLA response of **1a**−**5a** under high-laser-intensity excitation conditions, Figure 6c,d presents some representative OA Z-scans obtained under 220 and 200 MW/cm^2, at 1064 and 532 nm, respectively. As is shown, in all cases, a transmittance minimum is observed, indicative of RSA behavior.

In Figure 7, some representative "divided" Z-scans of **1a**−**5a** in DMF, all having 0.1 mg/mL concentration, are shown. Due to the negligible NLR response of DMF, the "divided" Z-scans reveal directly the response of **1a**−**5a**. As is shown, under 532 nm excitation, the NLR response of **1a**−**5a** was found to be relatively stronger than that under excitation at 1064 nm. In addition, in both cases, the NLR response of the hybrids was found to be larger than that of MoS_2, with **2a** exhibiting the strongest response. It is worth noting that the valley−peak transmittance configuration, i.e., sign of the NLR response, of **1a**−**5a** (i.e., self-focusing, $\gamma' > 0$) was found unaffected under both low- and high-laser intensities.

From the analyses of the OA and "divided" Z-scans obtained under 1064 and 532 nm excitation, using low- and high-incident laser intensities, the values of nonlinear absorption coefficient β, the nonlinear refractive index parameter γ', the corresponding imaginary and real parts of the third-order nonlinear susceptibility $\chi^{(3)}$, i.e., Im$\chi^{(3)}$ and Re$\chi^{(3)}$, and the $\chi^{(3)}$ values were determined for the different-concentration dispersions studied. They are summarized in Tables S1 and S2. To make comparisons easier, the values of Im$\chi^{(3)}$/c, Re$\chi^{(3)}$/c, and $\chi^{(3)}$/c for each different-concentration dispersion studied (i.e., the Im$\chi^{(3)}$, Re$\chi^{(3)}$, and $\chi^{(3)}$ normalized by the concentration c), were calculated as well. The averaged values of the normalized quantities of different-concentration dispersions for each MoS_2−PDI hybrid material **1a**−**5a** and MoS_2 are listed in Table 1, while they are schematically depicted in Figure 8.

From the inspection of the results of Table 1 and Figure 8, some general remarks can be done. So, at first, it was confirmed that the nonlinear absorption of **1a**−**5a** switches from SA (i.e., $\beta < 0$) to RSA (i.e., $\beta > 0$) increasing the laser excitation intensity, while the corresponding nonlinear refractive (NLR) response remains unaltered (i.e., self-focusing, $\gamma' > 0$). The same trends are also observed for MoS_2. In all cases, **1a** and **2a** (i.e., the hybrid materials with imide- and bay-substituted azobenzene PDIs **1** and **2**, respectively) exhibited the largest

Table 1. NLO Parameters of MoS_2−PDI Hybrid Materials 1a−5a Determined under Low- and High-Laser Intensity, 1064 and 532 nm, Laser Excitation Conditions

λ_{exc} (nm)	material	$\text{Im}\chi^{(3)}/c$ ($\times 10^{-13}$ esu mL/mg)	$\text{Re}\chi^{(3)}/c$ ($\times 10^{-13}$ esu mL/mg)	$\chi^{(3)}/c$ ($\times 10^{-13}$ esu mL/mg)	$\text{Im}\chi^{(3)}/c$ ($\times 10^{-13}$ esu mL/mg)	$\text{Re}\chi^{(3)}/c$ ($\times 10^{-13}$ esu mL/mg)	$\chi^{(3)}/c$ ($\times 10^{-13}$ esu mL/mg)
			low intensity			high intensity	
1064	**MoS_2**	−196.9 ± 10.2	182.7 ± 8.9	268.9 ± 9.4	115.2 ± 6.2	139.6 ± 7.8	181.1 ± 8.4
	1a	−172.5 ± 13.3	320.3 ± 29.9	364.7 ± 32.8	120.3 ± 10.3	276.0 ± 29.9	300.9 ± 32.8
	2a	−273.6 ± 19.0	405.4 ± 38.4	489.0 ± 43.3	96.5 ± 17.1	345.5 ± 40.0	358.8 ± 43.3
	3a	−200.9 ± 15.4	206.6 ± 23.2	291.8 ± 28.4	66.6 ± 6.2	132.5 ± 23.2	149.0 ± 20.6
	4a	−131.7 ± 10.3	235.7 ± 20.7	270.4 ± 23.0	67.9 ± 7.6	192.9 ± 27.6	212.7 ± 29.1
	5a	−159.2 ± 15.1	230.4 ± 29.4	288.4 ± 33.2	79.5 ± 8.3	202.7 ± 24.4	218.0 ± 26.6
532	**MoS_2**	−242.7 ± 18.7	716.7 ± 71.5	761.5 ± 73.7	90.2 ± 6.5	751.5 ± 58.5	757.0 ± 58.5
	1a	−359.8 ± 29.0	688.9 ± 53.2	777.5 ± 63.1	126.3 ± 17.0	634.1 ± 39.2	646.8 ± 47.3
	2a	−514.7 ± 57.4	363.5 ± 51.0	631.7 ± 76.0	127.0 ± 33.0	329.8 ± 38.0	352.7 ± 51.0
	3a	−159.1 ± 12.1	321.4 ± 34.3	355.1 ± 36.6	53.0 ± 5.5	283.0 ± 29.7	287.8 ± 30.2
	4a	−232.3 ± 23.9	289.8 ± 26.0	371.5 ± 33.5	85.9 ± 9.8	275.8 ± 23.5	288.9 ± 25.3
	5a	−248.4 ± 28.8	300.4 ± 29.0	389.9 ± 41.6	96.5 ± 28.4	300.4 ± 29.0	311.8 ± 39.7

NLO response among the studied MoS_2−PDI hybrid materials. In addition, the hybrids presenting absorption bands near the excitation wavelength were found to exhibit stronger NLO absorption and refraction. In that view, it must be added that the excitation of **1a**−**5a** at 532 nm resulted in a stronger NLO response. Furthermore, in the case of low-intensity excitation (see, e.g., Table 1), **1a** and **2a** were found to exhibit stronger NLO response than **3a**, **4a**, and **5a**, for both 1064 and 532 nm excitations, the latter hybrids exhibiting similar-magnitude NLO response. Regarding the comparison of the NLO response of the MoS_2−PDI hybrid materials **1a**−**5a** with MoS_2, **1a** and **2a** exhibited stronger response than MoS_2, when excited at 1064 and 532 nm, under both low- and high-laser intensities. **3a**, **4a**, and **5a** exhibited a similar response to that of MoS_2 under both low- and high-intensity excitations at 1064 nm. In contrast, their response was found to be lower than that of MoS_2 under both low- and high-intensity excitation at 532 nm.

For comparison of the switching behavior of the NLA response (i.e., from SA to RSA) of the MoS_2−PDI hybrid materials **1a**−**5a**, the variation of $\text{Im}\chi^{(3)}/c$ of different concentration dispersions of **1a**−**5a** with the laser intensity is presented in Figure 9. As is shown, the threshold intensity for switching from SA to RSA of **1a**−**5a** was found to be significantly higher than that of MoS_2, ranging between 150 and 250 MW/cm^2, depending on the hybrid material. Among the examined hybrid materials, **1a** and **2a** (i.e., the MoS_2−PDI hybrid materials with the imide- and bay-substituted PDIs **1** and **2**) exhibited the highest threshold intensity, i.e., ~200 and ~150 MW/cm^2 for 532 and 1064 nm excitations, respectively. In addition, **1a** and **2a** for incident laser intensities higher than 250−300 MW/cm^2 were found to exhibit RSA behavior, thus being suitable for optical limiting of more intense radiation. It is useful to add at this point that the switching of the NLA response of the MoS_2−PDI hybrid materials can be of interest for various optoelectronic and photonic applications, as it suggests their potential for multiple uses. For example, the SA behavior can be of interest for mode-locking-related applications, while RSA can be useful for optical limiting.

For obtaining a better insight into the NLA response of the MoS_2−PDI hybrid materials **1a**−**5a**, the energy bandgap, E_g, values of **1a**−**5a** were estimated via the Tauc method. They were found to range between 1.59 and 1.81 eV (see also Figure S10). Based on these values of E_g, the SA behavior of **1a**−**5a** under 532 nm (2.30 eV) excitation, can be understood in terms of efficient Pauli blocking process.[11] In the case of excitation at 1064 nm (1.17 eV), the SA response of **1a**−**5a** can be attributed to the presence of mid-bandgap (or defect states) that assist an 1 + 1 photon absorption process. It is reminded that the differential pulse voltammetry assays discussed above (see also Figures 4c and S8) are also in support of the presence of such bandgap states. These states are probably trap states, resulting mainly from the modification of the electronic structure of MoS_2 due to asymmetry at the edges of atomic planes and unsatisfied bonds between Mo and S atoms, as it has been discussed for some MoS_2 nanosheets.[11,46−49]

Concerning the nonlinear refraction of **1a**−**5a**, several physical origins can be evoked, associated with the instantaneous bound-electronic response (Kerr nonlinearity) or other noninstantaneous contributions, such as molecular reorientation, thermal effects, and free carrier refraction. In the present case, however, under ns excitation, the free carrier

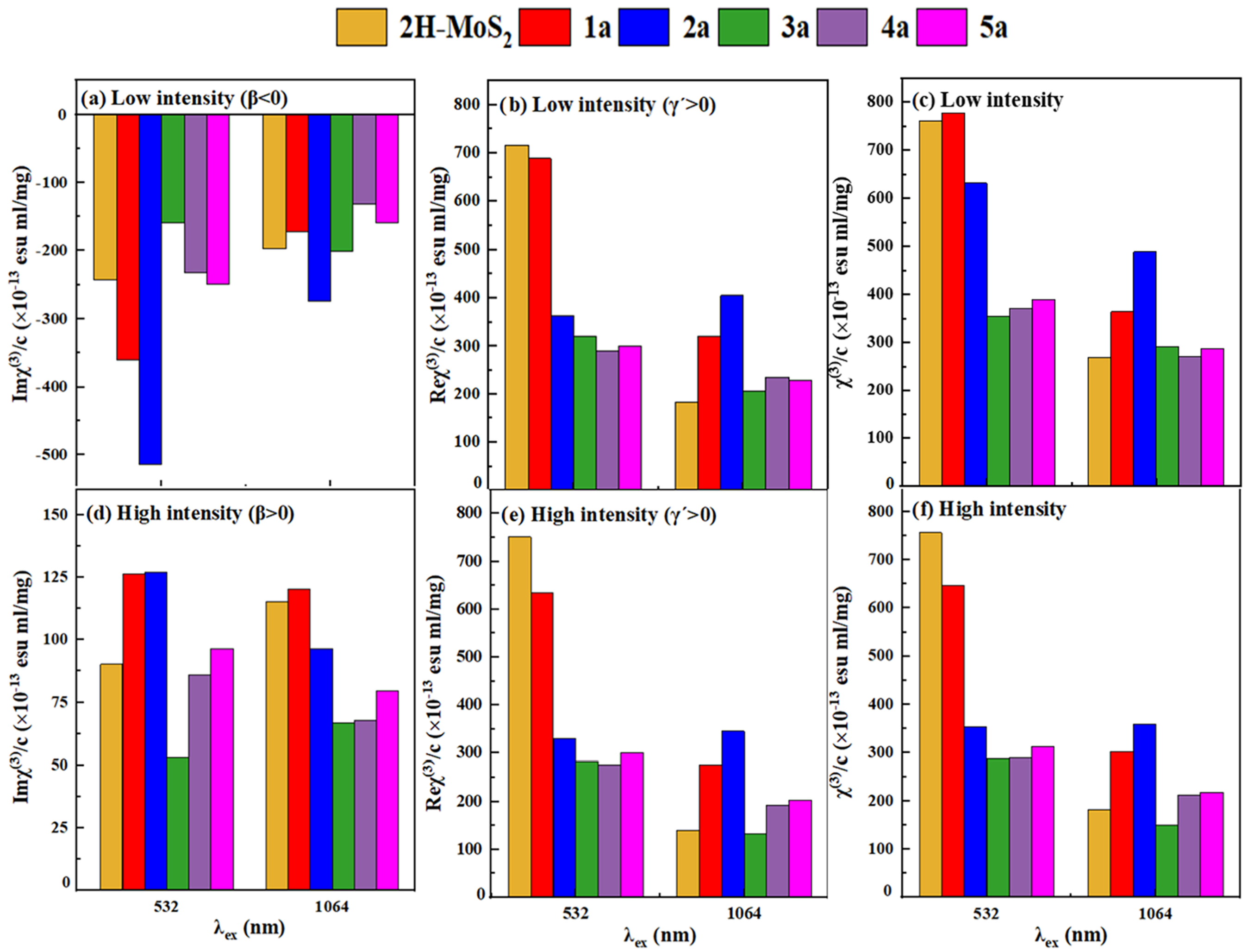

Figure 8. Determined values of Im$\chi^{(3)}$/c, Re$\chi^{(3)}$/c, and $\chi^{(3)}$/c of MoS_2−PDI hybrid materials **1a**−**5a** under (a−c) low- and (d−f) high-intensity, 4 ns, 1064 and 532 nm laser excitation.

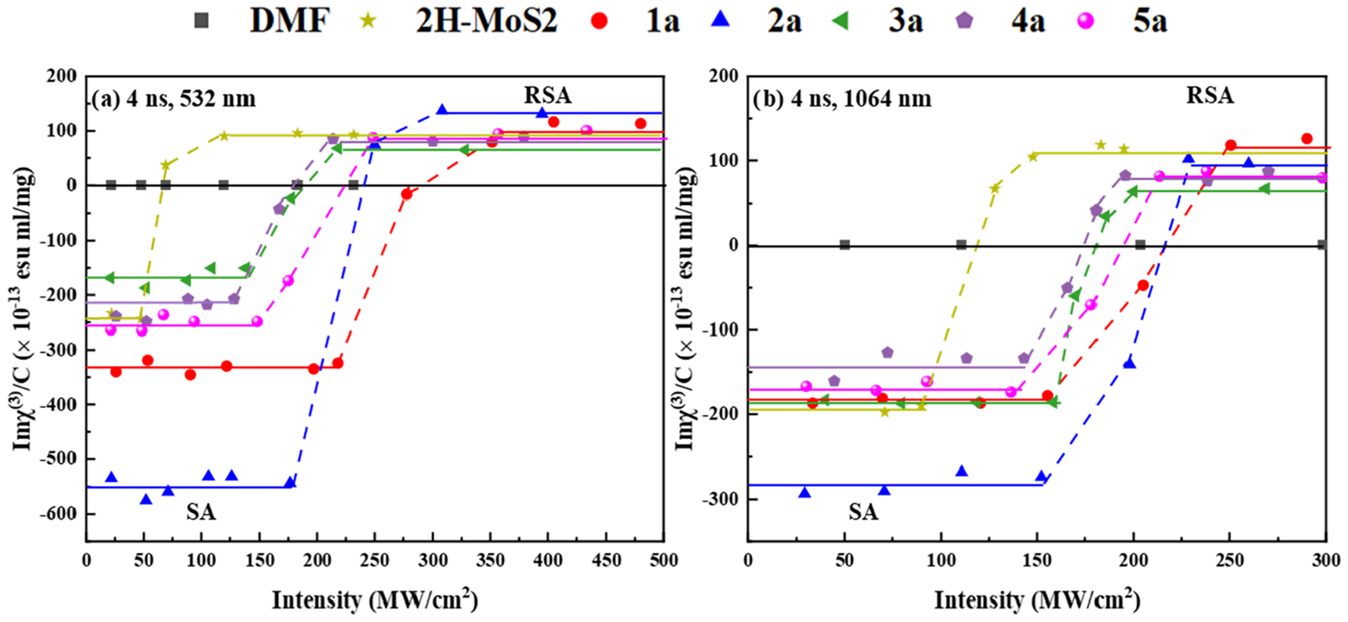

Figure 9. Variation of Im$\chi^{(3)}$/c of MoS_2−PDI hybrid materials **1a**−**5a** with the incident laser intensity under 4 ns, (a) 532 and (b) 1064 nm laser excitation.

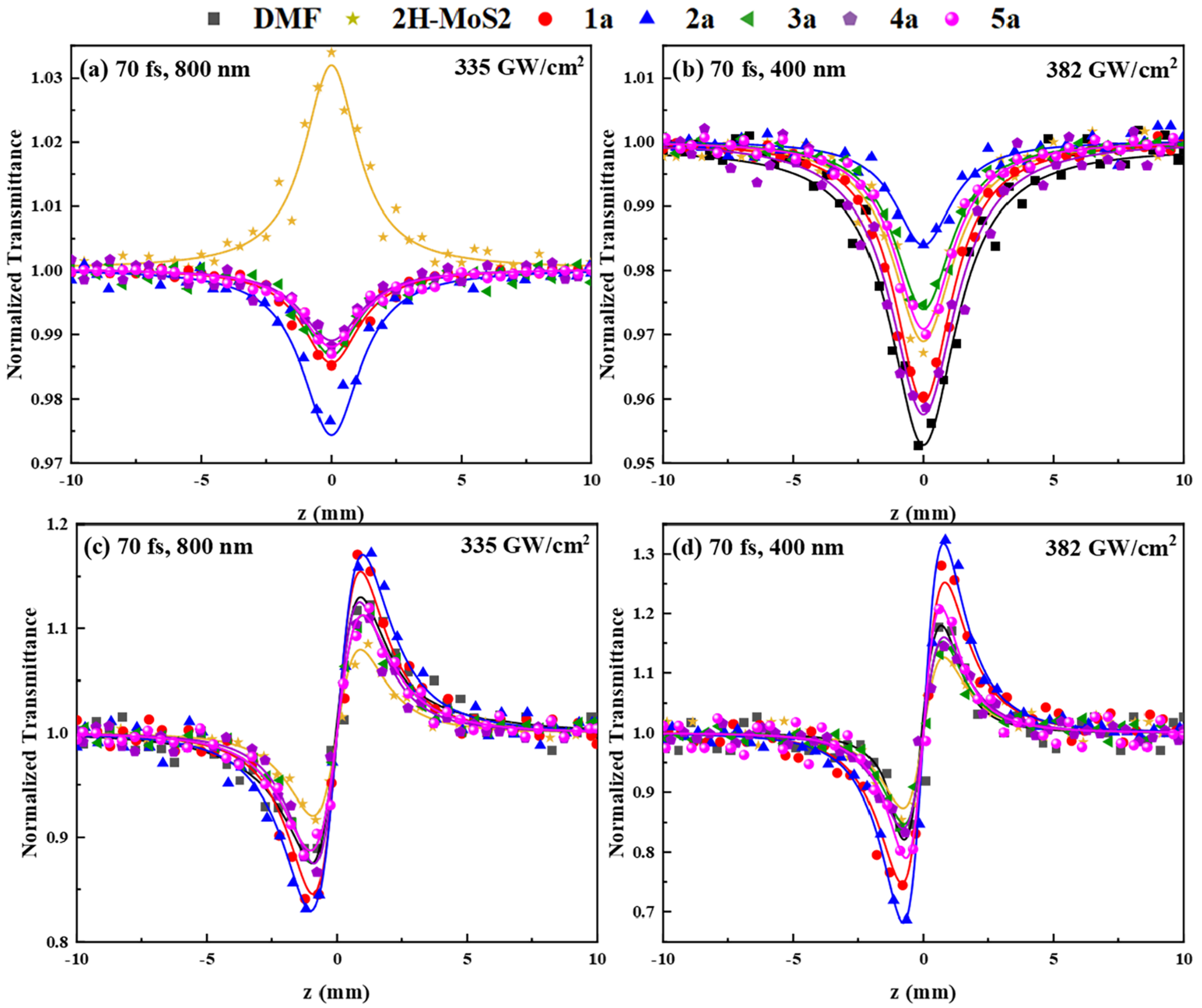

Figure 10. (a, b) OA and (c, d) "divided" Z-scans of MoS_2−PDI hybrid materials **1a**−**5a** in DMF (0.1 mg/mL), under 70 fs, 800 and 400 nm laser excitation.

refraction mechanism is expected to be the most efficient one.[11]

NLO Response under 70 fs, 800/400 nm Laser Excitation

Next, the experimental findings concerning the NLO response of the MoS_2−PDI hybrid materials **1a**−**5a** and exfoliated MoS_2 under 70 fs, 800 and 400 nm laser excitation are presented and discussed. First, their NLA response is presented. In Figure 10a,b some representative OA Z-scans of **1a**−**5a** and MoS_2 dispersions in DMF (0.1 mg/mL) are shown, obtained under 800 and 400 nm excitations, respectively. As can be seen in Figure 10a, under 800 nm excitation, the MoS_2 dispersion exhibited SA behavior, while the dispersions of **1a**−**5a** exhibited all RSA. The measurements were performed for intensities up to 260 GW/cm², as at higher intensities saturation of the OA Z-scans started to appear. Similar measurements of neat DMF exhibited negligible NLA for the range of laser intensities used.[27] Therefore, the OA Z-scans shown in Figure 10a reveal straightforwardly the NLA response of **1a**−**5a** and MoS_2, the former exhibiting RSA (i.e., $\beta>0$), and the latter SA (i.e., $\beta<0$). These findings demonstrate that the functionalization of MoS_2 with the PDI derivatives **1**−**5** results in switching its NLA response from SA to RSA.

Similar measurements performed using 400 nm excitation have shown that the dispersions of **1a**−**5a** and MoS_2 exhibited RSA behavior, as presented in Figure 10b. However, in this case, DMF exhibited sizable RSA (i.e., $\beta > 0$) as well.[27] However, the transmission minimum of the OA Z-scans of **1a**−**5a** and MoS_2 dispersions was found to be smaller than that of DMF, suggesting an opposite sign nonlinear absorption. So, for the determination of the NLO parameters of **1a**−**5a** and MoS_2, the contribution of DMF had to be considered accordingly. The measurements were performed at intensities up to 600 GW/cm². The results concerning the NLA responses of **1a**−**5a** and MoS_2 are shown in Figure S11. As is shown, under 400 nm excitation, both MoS_2 and the hybrid materials **1a**−**5a** were all found to exhibit SA behavior (i.e., $\beta <$ 0).

In the case of fs excitation, 800 nm (1.55 eV), the observed SA behavior of MoS_2 can be attributed to both the Pauli blocking mechanism and the efficient depletion of the ground state, due to the relatively much higher laser intensity used (compared to ns excitation).[50,51] However, in the case of hybrids, all exhibiting RSA behavior, a two-photon absorption process should be considered, since in this case, two photons are required to bridge the bandgap of **1a**−**5a** (i.e., ∼1.60−1.80 eV).[50] In the same spirit, under 400 nm (3.10 eV) excitation, the observed SA behavior of MoS_2 and **1a**−**5a** can also be understood by evoking the Pauli blocking mechanism.

Concerning the NLR response of exfoliated MoS_2 and the MoS_2−PDI hybrid materials **1a**−**5a** under fs laser excitation, they were all found exhibiting self-focusing behavior (*i.e.*, $\gamma' > 0$) under both 800 and 400 nm excitation, as indicated by the corresponding divided Z-scans of Figure 10c,d. Again, since DMF exhibited important NLR response, i.e., self-focusing, as can be seen in Figure 10c,d, its contribution has been measured separately and considered accordingly for the determination of the NLR response of **1a**−**5a** and MoS_2.[27] It is important to add that under fs excitation, the observed NLR response of **1a**−**5a** and MoS_2 is due to the instantaneous bound-electronic response (i.e., Kerr-type nonlinearity).[52]

From the analysis of the OA and "divided" Z-scans obtained under 70 fs, 800 and 400 nm excitation, the values of the different NLO parameters of **1a**−**5a** and MoS_2 studied, were deduced and are summarized in Table S3 for all of the different-concentration dispersions studied. To facilitate comparison, the concentration-normalized values of $\mathrm{Im}\chi^{(3)}/c$, $\mathrm{Re}\chi^{(3)}/c$, and $\chi^{(3)}/c$ are presented in Table 2 and are schematically depicted in Figure 11. As can be seen, **2a** and **1a** exhibit the largest NLO response (both absorptive and refractive) among the hybrids, being also larger than that of MoS_2, at both excitation wavelengths; the NLO response of **3a**−**5a** were found to be very similar to that of MoS_2. Interestingly, PDIs **2** and **1** were found to exhibit the largest NLO response among the PDIs studied in a previous work.[27] The larger NLO response of **2a** and **1a** is most probably due to the more efficient electron transfer occurring in these hybrids, in agreement with the photoluminescence emission spectroscopy measurements reported elsewhere.[46,50,53,54] It is interesting to note that the enhancement of the total NLO response of **2a** (i.e., $\chi^{(3)}/c$) is mainly related to the enhancement of its NLR response (i.e., $\mathrm{Re}\chi^{(3)}/c$), which in turn is also due to the more efficient electron transfer occurring in this MoS_2−PDI hybrid material, due to the presence of PDI **2** (i.e., the bay-substituted azobenzene PDI).

Table 2. Determined NLO Parameters of 2H-MoS_2 and MoS_2−PDI Hybrid Materials 1a−5a under 70 fs Laser Excitation

λ_{exc} (nm)	material	$\mathrm{Im}\chi^{(3)}/c$ ($\times 10^{-16}$ esu mL/mg)	$\mathrm{Re}\chi^{(3)}/c$ ($\times 10^{-16}$ esu mL/mg)	$\chi^{(3)}/c$ ($\times 10^{-16}$ esu mL/mg)
800	**MoS_2**	−13.5 ± 3.0	9.2 ± 1.2	25.1 ± 3.1
	1a	24.8 ± 2.8	28.1 ± 3.6	37.6 ± 4.4
	2a	39.6 ± 4.4	32.2 ± 3.8	51.3 ± 5.8
	3a	16.9 ± 2.0	19.6 ± 2.4	26.1 ± 3.1
	4a	18.2 ± 2.1	21.2 ± 2.2	28.1 ± 3.0
	5a	19.0 ± 2.1	26.2 ± 3.6	32.3 ± 3.7
400	**MoS_2**	−13.8 ± 1.0	36.8 ± 4.2	39.1 ± 4.4
	1a	−27.0 ± 2.7	67.4 ± 7.4	72.3 ± 8.2
	2a	−60.9 ± 6.1	96.4 ± 9.2	114.6 ± 11.2
	3a	−10.8 ± 1.3	38.8 ± 4.2	40.4 ± 4.5
	4a	−9.4 ± 1.2	41.5 ± 4.8	41.5 ± 4.9
	5a	−10.2 ± 1.6	47.4 ± 5.	46.4 ± 5.8

For comparison of the NLO response of the MoS_2−PDI hybrid materials **1a**−**5a** with other MoS_2-based hybrid materials and to better assess their performance, some results reported in the literature are presented below. To facilitate comparison, and make them more straightforward, only results assessing dispersions of these materials and obtained under ns and/or fs laser excitation conditions are discussed. In this frame, the NLO-absorptive response and the optical-limiting performance of some MoS_2 nanosheets covalently functionalized with poly(*N*-vinylcarbazole) (e.g., MoS_2−PVK) dispersed in DMF, employing 6 ns, 532 and 1064 nm laser pulses, were studied.[55] It was found that MoS_2−PVK exhibited superior nonlinear absorption coefficient, β_{eff}, under both visible and infrared excitation, compared to pristine MoS_2 and/or the MoS_2/PVK blends (all dispersed in DMF), while their nonlinear absorption behavior changed from SA (at low incident laser intensities), to RSA, at higher intensities. Moreover, β_{eff} values of 10^{-11}−10^{-10} m/W, similar to those measured for the current MoS_2−PDI hybrids, were reported. In a similar work, the nonlinear absorption behavior of some MoS_2 nanosheets covalently functionalized with polyacrylonitrile (PAN) (e.g., MoS_2−PAN) dispersed in DMF, under 6 ns, 532 and 1064 nm laser excitation, was studied.[56] Again, the nonlinear absorption of MoS_2−PAN changed from SA to RSA by increasing the incident laser intensity, while the reported values of β_{eff} were of similar magnitude to those of MoS_2−PVK materials and similar to those of the MoS_2−PID hybrids studied in the present work. In addition, MoS_2 covalently functionalized with 6-(9*H*-carbazol-9-yl)hexane-1-thiol (e.g., MoS_2−CHT) dispersed in DMF found that the SA observed at low-laser intensities changes to RSA at higher-laser intensities, showing similar-magnitude β_{eff} (i.e., 10^{-11}−10^{-10} m/W).[57] For MoS_2/ZnPc composites, the nonlinear absorption behavior change from SA to RSA at higher-laser intensities was reported, while the determined β_{eff} values were $\sim 10^{-9}$ m/W, i.e., about an order of magnitude larger compared to the current MoS_2−PDI hybrids.[58] In a more recent work, the nonlinear absorption of an organic−inorganic hybrid, carmine−MoS_2, by means of 9 ns, 532 nm laser excitation, was studied, and a value of $\sim 10^{-12}$ m/W for the nonlinear absorption coefficient β, i.e., slightly lower than that for MoS_2−PDI hybrids **1a**−**5a**, was found.[59] Finally, the NLO properties of MoS_2 covalently functionalized with porphyrin exhibited RSA behavior under 800 nm excitation and changing to SA when excited at 515 nm.[50] It should be remembered that the current MoS_2−PDI hybrids **1a**−**5a** exhibit RSA behavior under 800 nm and SA behavior when excited at 400 nm (see e.g., Tables 2 and S3). The β_{eff} values of MoS_2−porphyrin were $\sim 10^{-13}$ and $\sim 10^{-14}$ m/W, under 800 and 514 nm excitations, respectively, i.e., of similar magnitude to those of MoS_2−PDI hybrids **1a**−**5a**. In addition, the MoS_2−porphyrin nanohybrids were found to exhibit self-focusing behavior, i.e., a positive nonlinear refractive index, n_2, of $\sim 3.1 \times 10^{-19}$ m^2/W, in very good agreement with the findings of the present work on the MoS_2−PDI hybrids **1a**−**5a**.

EXPERIMENTAL SECTION

General

Steady-state emission spectra were recorded on a FluoroLog-3 Jobin-Yvon-Spex spectrofluorometer (model GL3−21). Picosecond time-resolved fluorescence spectra were measured by the time-correlated single-photon counting (TCSPC) method on a NanoLog spectrofluorometer (Horiba Jobin Yvon), by using a laser diode as an

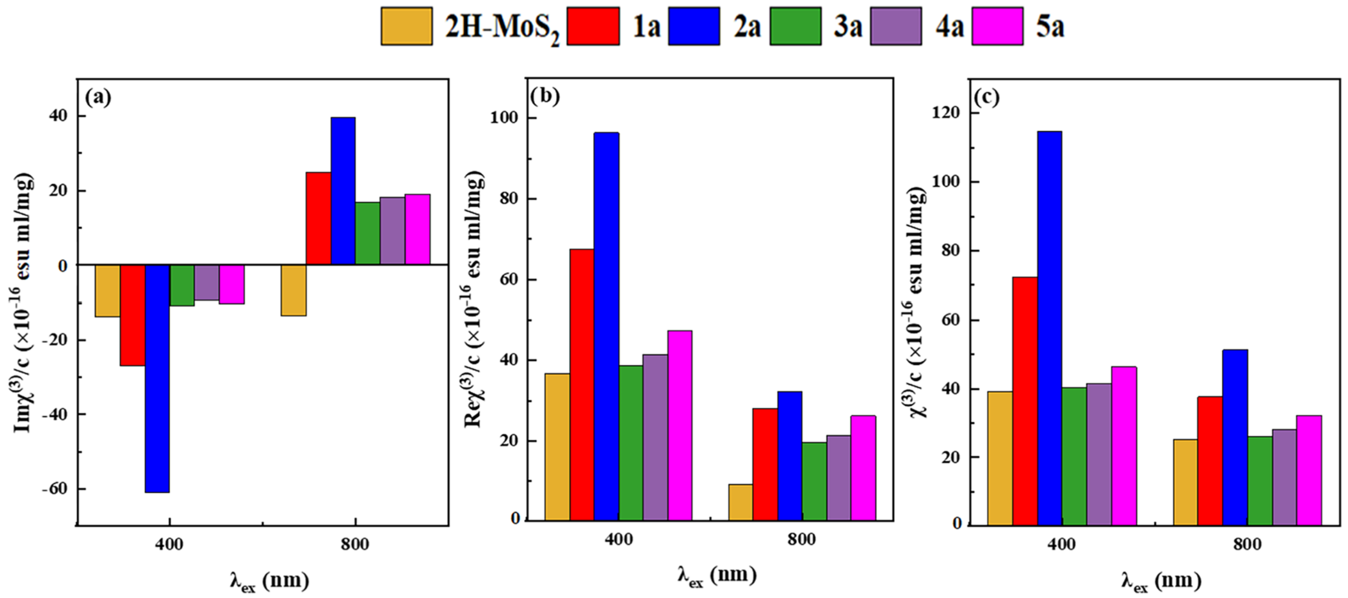

Figure 11. Determined values of (a) Im$\chi^{(3)}$/c, (b) Re$\chi^{(3)}$/c, and (c) $\chi^{(3)}$/c of the MoS_2−PDI hybrid materials **1a**−**5a** and MoS_2 under 70 fs and 800 and 400 nm laser excitation.

excitation source (NanoLED, 375 nm) and a UV−vis detector TBX-PMT series (250−850 nm) from Horiba JobinYvon. Mid-infrared spectra in the region 500−4500 cm^{-1} were obtained on a Fourier transform IR spectrometer (Equinox 55 from Bruker Optics) equipped with a single-reflection diamond ATR accessory (DuraSamp1IR II from SensIR Technologies). A drop of the solution was placed on the diamond surface, followed by evaporation of the solvent in a stream of nitrogen, before recording the spectrum. Typically, 100 scans were acquired at 2 cm^{-1} resolution. Micro-Raman scattering measurements were performed at room temperature in the backscattering geometry using a Renishaw inVia Raman microscope equipped with a CCD camera and a Leica microscope. A 2400 lines mm^{-1} grating was used for all measurements, providing a spectral resolution of ± 1 cm^{-1}. As an excitation source, the Ar^+ laser (633 nm with less than 2.65 mW/cm^2 laser power and with less than of 10% of 4.5 mW/cm^2 laser power) was used. Measurements were taken with 15 s of exposure times with varying numbers of accumulations. The laser spot was focused on the sample surface using a long working distance 50× objective. Raman spectra were collected on numerous spots on the sample and recorded with a Peltier cooled CCD camera. Raman spectral mapping analysis was carried out with Renishaw's Wire. Thermogravimetric analysis was performed using a TA Instruments TGA Q500 V20.2 Build 27 in a nitrogen (purity >99.999%) inert atmosphere. Cyclic voltammograms were recorded on an Autolab PGSTAT128N potentiostat/galvanostat equipped with a dual-mode bipotentiostat (BA module) electrochemical analyzer using a three-electrode system. A platinum button electrode was used as the working electrode. A platinum cloth served as the counter electrode and a platinum wire was used as the reference electrode. All solutions were purged with nitrogen gas prior to electrochemical and spectral measurements. For transmission electron microscopy (TEM) studies, the samples were drop-cast on holey C-coated Cu grids. High-resolution STEM (HRSTEM) imaging and STEM- energy-dispersive X-ray spectroscopy (EDS) analyses were performed in a probe-corrected Thermo Fisher Scientific Titan Low Base, working at 120 kV and equipped with a high-brightness field-emission gun (XFEG) and an Oxford Instruments Ultim X-MaxN 100TLE detector for the EDS measurements.

NLO Measurements

For the measurement of NLO properties of the studied 2H-MoS_2 and MoS_2−PDI hybrid materials **1a**−**5a**, several different-concentration dispersions in DMF (analytical grade) were prepared. The concentrations of the dispersions were adjusted to correspond to absorbances suitable for Z-scan measurements at different laser excitation wavelengths (i.e., 1064, 800, 532, and 400 nm) for each dispersed material, i.e., absorbance values lower than 0.3−0.4 in general. After sonication of the prepared dispersions for ∼30 min, they have been left to settle, and from the supernatant a portion was collected and placed in 1 mm thick quartz cells for the measurement of their UV−vis−NIR absorption spectra and Z-scan measurements. The absorption spectra were routinely checked prior to, during, and after the NLO measurements using a double-beam spectrophotometer (Jasco V-670) to ensure the stability of their concentration and that no photodegradation has occurred during the NLO measurements where the samples were exposed to high-laser intensities.

For the Z-scan experiments, two different laser sources were employed. A 4 ns Q-switched Nd/YAG laser (EKSPLA NT 342/3/UVE/AW) operating at its fundamental at 1064 nm and at its second harmonic at 532 nm, with a repetition rate between 1 and 10 Hz, and a fs CPA mode-locked Ti/sapphire laser system (Trident X, Amplitude Technologies) operating at its fundamental at 800 nm and its second harmonic at 400 nm, with pulse durations of 70 and 50 fs, respectively, at a repetition rate of 10 Hz. The duration of the femtosecond laser pulses was measured by an autocorrelator (Single Shot Autocorrelator (SSA) Bonsai, Amplitude Technologies). In all cases, the laser beam was focused onto the samples by means of a 20 cm focal length quartz lens. The beam radii at the focus, for all wavelengths employed, were measured using a CCD camera; they were found to be approximately (30 ± 4) and (18 ± 4) μm, at 1064 and 532 nm, and (25 ± 5) and (20 ± 5) μm, at 800 and 400 nm, respectively.

Z-Scan

The NLO response of the 2H-MoS_2 and the MoS_2−PDI hybrid materials **1a**−**5a** was investigated by means of the Z-scan technique.[60] Z-scan, using a single laser beam, is relatively simple experimentally, while it allows for the simultaneous determination of both the sign and the magnitude of the nonlinear absorption coefficient β and the nonlinear refractive index parameter γ', from a single measurement. According to this technique, the normalized transmittance of a sample exposed to variable laser-intensity levels is measured as it moves along the propagation direction (z-axis) of a focused laser beam. The transmittance of the sample is measured simultaneously in two different experimental configurations called "Open-Aperture" (OA) and "Closed-Aperture" (CA) Z-scans, respectively. As the sample approaches the focal plane of the laser beam (i.e., at z = 0), the intensity of the laser beam becomes strong enough, inducing the NLO absorption and refraction of the sample, resulting in the modification of its transmittance.

In the OA Z-scan configuration, the entire laser beam transmitted through the sample is collected by a lens and measured by a detector (e.g., PMT or photodiode). The corresponding recording can exhibit a transmission maximum around the focal plane or a transmission minimum. The former indicates saturable absorption behavior (SA, $\beta < 0$), while the latter suggests reverse-saturable absorption behavior (RSA, $\beta > 0$), respectively. From the OA Z-scan recording, the nonlinear coefficient β can be determined by fitting the experimental OA with eq 1

$$T(z) = \frac{1}{\sqrt{\pi}\left(\frac{\beta I_o L_{\mathrm{eff}}}{1+\left(\frac{z}{z_0}\right)^2}\right)} \int_{-\infty}^{+\infty} \ln\left[1 \,\middle|\, \frac{\beta I_o L_{\mathrm{eff}}}{1+\left(\frac{z}{z_0}\right)^2} \mathrm{e}^{-t}\right] \mathrm{d}t \tag{1}$$

where $T(z)$ denotes the sample's transmittance at each z-position, z_0 is the Rayleigh length, I_0 is the laser intensity at the focal plane, and L_{eff} is the sample's effective length at the excitation wavelength.

In the CA Z-scan configuration, only the central part of the laser beam transmitted through the sample is measured, after it has passed through an aperture positioned in the far field in front of the detector. The CA Z-scan recording can exhibit either a prefocal transmission minimum followed by a postfocal maximum or vice versa, indicating a self-focusing ($\gamma' > 0$) or self-defocusing ($\gamma' < 0$) behavior, respectively. In the case where significant NLO absorption is present, to remove its influence on the CA Z-scan recording, the latter is divided by the corresponding OA Z-scan, yielding the so-called "divided" Z-scan. The nonlinear refractive index parameter γ', in both cases, can be derived by fitting the experimental CA or the "divided" Z-scan recordings, respectively, with eq 2

$$T(z) = 1 - \frac{4\gamma' k I_0 L_{\mathrm{eff}}\left(\frac{z}{z_0}\right)^2}{\left[1+\left(\frac{z}{z_0}\right)^2\right]\left[9+\left(\frac{z}{z_0}\right)^2\right]} \tag{2}$$

where k denotes the excitation wavenumber.

Then, from the thus-determined β and γ', the imaginary, $\mathrm{Im}\chi^{(3)}$, and the real, $\mathrm{Re}\chi^{(3)}$, parts of third-order susceptibility $\chi^{(3)}$, can be deduced using eqs 3 and 4, respectively

$$\mathrm{Im}\,\chi^{(3)}(\mathrm{esu}) = 10^{-7}\frac{\mathrm{c}^2\mathrm{n}_0^2\beta}{96\pi^2\omega} \tag{3}$$

$$\mathrm{Re}\chi^{(3)}(\mathrm{esu}) = 10^{-6}\frac{\mathrm{c}\mathrm{n}_0^2\gamma'}{480\pi^2} \tag{4}$$

where c is the speed of light, n_0 is the linear refractive index, and ω is the frequency of laser radiation.

Exfoliated MoS_2

Bulk MoS_2 (150 mg) was dispersed in chlorosulfonic acid and sonicated for 1 h at room temperature. The solution was left stirring for a week and occasionally sonicated for 1 min. Cold water was then added to the solution under stirring, drop by drop, and with extreme care. *Caution: please note that the reaction is explosive and releases gaseous HCl.* Next, the mixture was filtered by using a PTFE filter (0.2 μm pore size) and washed with a substantial amount of methanol and acetone. The solid compound was added to 500 mL of *N*-methyl pyrrolidone and sonicated for 1 h (tip sonication at 30% amplitude (100% of 200 W)) and left under stirring for 24 h. Then, the supernatant was filtered over a PTFE filter (0.2 μm pore size) and washed with a large amount of methanol, acetone, and dichloromethane (yield: 30−40%).

MoS_2−COOH. Exfoliated MoS_2 (200 mg) was sonicated in DMF for 20 min. Then, lipoic acid (50 mg) was added, and the reaction mixture was stirred at 70 °C for 1 week with occasional sonication. Then, the supernatant was filtered over a PTFE membrane (0.2 μm pore size) and washed with a large amount of methanol, acetone, and dichloromethane.

MoS_2−PDI Hybrid Materials 1a−5a: General Procedure. In a round-bottom flask, MoS_2−COOH (55 mg) was sonicated in dry dichloromethane (20 mL) for 1 h at room temperature. Then, EDC·HCl (20 mg), DMAP, and PDI derivatives **1**−**5** (20 mg) were added, and the reaction mixture was sonicated for 1 h and then stirred for 6 h. Then, 1 drop of DIPEA was added, and the reaction mixture was sonicated for 5 min and then heated at 50 °C under vigorous stirring for 7 days. During this period, the reaction was occasionally sonicated, and every 2 days small quantities of EDC·HCl (5 mg) and DMAP (5 mg) were added. Afterward, the reaction mixture was left to reach room temperature and filtered over a PTFE membrane (0.2 μm pore size), and the solid residue was extensively washed with methanol and dichloromethane to yield the MoS_2−PDI hybrid materials **1a**−**5a** as dark-gray powders.

CONCLUSIONS

In the present work, five MoS_2−PDI hybrid materials, **1a**−**5a**, were synthesized via covalent bonding of different imide- and bay-modified PDI derivatives on liquid exfoliated semiconducting 2H-MoS_2 nanosheets. The synthesized MoS_2-based hybrid materials were comprehensively characterized by IR and Raman spectroscopy as well as UV−vis absorption and photoluminescence emission spectroscopy. In addition, their thermal and redox properties were assessed by TGA and electrochemistry, while their structural and chemical composition analyses were performed by STEM imaging coupled with EDS. Furthermore, the NLO response of the MoS_2−PDI hybrid materials **1a**−**5a** was investigated in detail, under both 4 ns and 70 fs laser pulses, at different excitation wavelengths. It was found that the NLO response can be tuned through the selection of the modified PDI derivative. Additionally, it was shown that their nonlinear absorptive response can be tuned as well, as they can exhibit saturable or reverse-saturable absorption when irradiated under low- or high-laser intensity, respectively. Overall, the present results indicate the great potential of the MoS_2−PDI hybrid materials **1a**−**5a** for different optoelectronic and photonic applications related to optical devices and signal conversion.

ASSOCIATED CONTENT

Supporting Information

The Supporting Information is available free of charge at https://pubs.acs.org/doi/10.1021/acsami.5c25463.

> Raman spectra and maps; IR spectra; TGA graphs; STEM-HAADF images and STEM-EDS analysis; UV−vis spectra; PL spectra; SWV graphs; energy diagram; Tauc plot diagram; OA Z-scans; and NLO parameters (PDF)

AUTHOR INFORMATION

Corresponding Authors

Fernando Fernández-Lázaro − *Área de Química Orgánica, Instituto de Bioingeniería, Universidad Miguel Hernández de Elche, Elche 03202, Spain;* orcid.org/0000-0002-4598-6024; Email: fdofdez@umh.es

Raul Arenal − *Instituto de Nanociencia y Materiales de Aragón (INMA), CSIC-Universidad de Zaragoza, Zaragoza 50009, Spain; Laboratorio de Microscopías Avanzadas (LMA), Universidad de Zaragoza, Zaragoza 50018, Spain;*

ARAID Foundation, Zaragoza 50018, Spain; orcid.org/0000-0002-2071-9093; Email: arenal@unizar.es

Stelios Couris − *Department of Physics, University of Patras, 26504 Patras, Greece; Institute of Chemical Engineering Sciences (ICE-HT), Foundation for Research and Technology-Hellas (FORTH), Patras, 26504 Patras, Greece;* Email: couris@upatras.gr

Nikos Tagmatarchis − *Theoretical and Physical Chemistry Institute, National Hellenic Research Foundation, Athens 11635, Greece;* orcid.org/0000-0001-7590-4635; Email: tagmatar@eie.gr

Authors

Eleni Nikoli − *Theoretical and Physical Chemistry Institute, National Hellenic Research Foundation, Athens 11635, Greece*

Ruben Canton-Vitoria − *Theoretical and Physical Chemistry Institute, National Hellenic Research Foundation, Athens 11635, Greece;* orcid.org/0000-0003-0595-0323

Georgios Skentzos − *Department of Physics, University of Patras, 26504 Patras, Greece*

Efrosyni Pramatioti − *Department of Physics, University of Patras, 26504 Patras, Greece*

Nathalie Zink-Lorre − *Área de Química Orgánica, Instituto de Bioingeniería, Universidad Miguel Hernández de Elche, Elche 03202, Spain;* orcid.org/0000-0003-3081-995X

Ana Maria Gutiérrez-Vílchez − *Area de Química Orgánica, Instituto de Bioingeniería, Universidad Miguel Hernández de Elche, Elche 03202, Spain;* orcid.org/0000-0002-9310-4022

Complete contact information is available at:
https://pubs.acs.org/10.1021/acsami.5c25463

Author Contributions

○E.N., R.C.V., G.S., and E.P. contributed equally to this work.

Funding

The open access publishing of this article is financially supported by HEAL-Link.

Notes

The authors declare no competing financial interest.

ACKNOWLEDGMENTS

Financial support by the Hellenic Foundation for Research and Innovation HFRI under the “2nd Call for HFRI Research Projects to support Faculty Members and Researchers,” Project Number: 2482, is acknowledged. F.F.-L. thanks the Grant PID2022-140315NB-I00 funded by MICIU/AEI/10.13039/501100011033 and by ERDF/EU. F.F.-L. is also indebted to the Generalitat Valenciana (CIPROM/2021/059) and the Advanced Materials program by MCIN with funding from the European Union NextGenerationEU (PRTR-C17.I1) and Generalitat Valenciana (MFA/2022/028). R.A. acknowledges funding from the Spanish MICIU with funding from the European Union NextGeneration EU (PRTR-C17.I1) promoted by the Government of Aragon and by the Spanish MICIU (PID2023-151080NB-I00/AEI/10.13039/501100011033 and CEX2023-001286-S MICIU/AEI/10.13039/501100011033), as well as from the Government of Aragon (DGA) through the project E13 23R. The TEM studies were conducted at the Laboratorio de Microscopías Avanzadas (LMA), Universidad de Zaragoza, Spain.

REFERENCES

(1) Mueller, T.; Malic, E. Exciton Physics and Device Application of Two-Dimensional Transition Metal Dichalcogenide Semiconductors. *npj 2D Mater. Appl.* **2018**, *2*, No. 29, DOI: 10.1038/s41699-018-0074-2.

(2) Mak, K. F.; Lee, C.; Hone, J.; Shan, J.; Heinz, T. F. Atomically Thin MoS$_2$: A New Direct-Gap Semiconductor. *Phys. Rev. Lett.* **2010**, *105*, No. 136805.

(3) Xu, J.; Peng, Y.; Jiang, J.; Qian, S.; Jiang, L. Nonlinear Optical Bistability Based on Epsilon-near-Zero Mode in near-Infrared Band. *Opt. Lett.* **2023**, *48*, 3235−3238.

(4) Wang, Y.; Ghotbi, M.; Das, S.; Dai, Y.; Li, S.; Hu, X.; Gan, X.; Zhao, J.; Sun, Z. Difference Frequency Generation in Monolayer MoS$_2$. *Nanoscale* **2020**, *12*, 19638−19643.

(5) Zhou, K. G.; Zhao, M.; Chang, M. J.; Wang, Q.; Wu, X. Z.; Song, Y.; Zhang, H. L. Size-Dependent Nonlinear Optical Properties of Atomically Thin Transition Metal Dichalcogenide Nanosheets. *Small* **2015**, *11*, 694−701.

(6) Zhao, M.; Chang, M. J.; Wang, Q.; Zhu, Z. T.; Zhai, X. P.; Zirak, M.; Moshfegh, A. Z.; Song, Y. L.; Zhang, H. L. Unexpected Optical Limiting Properties from MoS$_2$ Nanosheets Modified by a Semiconductive Polymer. *Chem. Commun.* **2015**, *51*, 12262−12265.

(7) Dong, N.; Li, Y.; Feng, Y.; Zhang, S.; Zhang, X.; Chang, C.; Fan, J.; Zhang, L.; Wang, J. Optical Limiting and Theoretical Modelling of Layered Transition Metal Dichalcogenide Nanosheets. *Sci. Rep.* **2015**, *5*, No. 14646.

(8) Wang, K.; Wang, J.; Fan, J.; Lotya, M.; O'Neill, A.; Fox, D.; Feng, Y.; Zhang, X.; Jiang, B.; Zhao, Q.; Zhang, H.; Coleman, J. N.; Zhang, L.; Blau, W. J. Ultrafast Saturable Absorption of Two-Dimensional MoS$_2$ Nanosheets. *ACS Nano* **2013**, *7*, 9260−9267.

(9) Wang, K.; Feng, Y.; Chang, C.; Zhan, J.; Wang, C.; Zhao, Q.; Coleman, J. N.; Zhang, L.; Blau, W. J.; Wang, J. Broadband Ultrafast Nonlinear Absorption and Nonlinear Refraction of Layered Molybdenum Dichalcogenide Semiconductors. *Nanoscale* **2014**, *6*, 10530−10535.

(10) Wen, X.; Gong, Z.; Li, D. Nonlinear Optics of Two-Dimensional Transition Metal Dichalcogenides. *InfoMat* **2019**, *1*, 317−337.

(11) Stavrou, M.; Chazapis, N.; Nikoli, E.; Arenal, R.; Tagmatarchis, N.; Couris, S. Crystalline Phase Effects on the Nonlinear Optical Response of MoS$_2$ and WS$_2$ Nanosheets: Implications for Photonic and Optoelectronic Applications. *ACS Appl. Nano. Mater.* **2022**, *5*, 16674−16686.

(12) Stangel, C.; Nikoli, E.; Tagmatarchis, N. Transition Metal Dichalcogenides Interfacing Photoactive Molecular Components for Managing Energy Conversion Processes. *Adv. Energy Sustainability Res.* **2022**, *3*, No. 2200097.

(13) Würthner, F. Perylene Bisimide Dyes as Versatile Building Blocks for Functional Supramolecular Architectures. *Chem. Commun.* **2004**, *4*, 1564−1579.

(14) Fernández-Lázaro, F.; Zink-Lorre, N.; Sastre-Santos, Á. Perylenediimides as Non-Fullerene Acceptors in Bulk-Heterojunction Solar Cells (BHJSCs). *J. Mater. Chem. A* **2016**, *4*, 9336−9346.

(15) Li, C.; Wonneberger, H. Perylene Imides for Organic Photovoltaics: Yesterday, Today, and Tomorrow. *Adv. Mater.* **2012**, *24*, 613−636.

(16) Zink-Lorre, N.; Font-Sanchis, E.; Sastre-Santos, Á.; Fernández-Lázaro, F. Perylenediimides as More Than Just Non-Fullerene Acceptors: Versatile Components in Organic, Hybrid and Perovskite Solar Cells. *Chem. Commun.* **2020**, *56*, 3824−3838.

(17) Guide, M.; Pla, S.; Sharenko, A.; Zalar, P.; Fernández-Lázaro, F.; Sastre-Santos, Á.; Nguyen, T. Q. A Structure-Property-Performance Investigation of Perylenediimides as Electron Accepting Materials in Organic Solar Cells. *Phys. Chem. Chem. Phys.* **2013**, *15*, 18894−18899.

(18) Zhan, X.; Zhang, J.; Tang, S.; Lin, Y.; Zhao, M.; Yang, J.; Zhang, H. L.; Peng, Q.; Yu, G.; Li, Z. Pyrene Fused Perylene Diimides: Synthesis, Characterization and Applications in Organic

Field-Effect Transistors and Optical Limiting with High Performance. *Chem. Commun.* **2015**, *51*, 7156−7159.

(19) Mariz, I. F. A.; Raja, S.; Silva, T.; Almeida, S.; Torres, É.; Baleizão, C.; Maçôas, E. Two-Photon Absorption of Perylene-3,4,9,10-Tetracarboxylic Acid Diimides: Effect of Substituents in the Bay. *Dyes Pigm.* **2021**, *193*, No. 109470.

(20) Hussain, W.; Ali, H. S.; Iqbal, M. S.; Bashir, M. R.; Khan, M. A.; Hanif, M.; Sandali, Y.; Irfan, A.; Li, H. Exploring Nonlinear Optical Properties of Perylene Diimide and Biomolecules Complexes: A Computational Supramolecular Study. *Theor. Chem. Acc.* **2024**, *143*, No. 27.

(21) Wang, L.; Liu, Y. L.; Li, Q. J.; Chen, S. H.; He, D.; Wang, M. S. Assembling of Perylene, Naphthalene, and Pyromellitic Diimide-Based Materials and Their Third-Order Nonlinear Optical Properties. *J. Phys. Chem. A* **2022**, *126*, 870−878.

(22) Jerca, F. A.; Jerca, V. V.; Hoogenboom, R. Advances and Opportunities in the Exciting World of Azobenzenes. *Nat. Rev. Chem.* **2022**, *6*, 51−69.

(23) Dudek, M.; Kaczmarek-Kędziera, A.; Deska, R.; Trojnar, J.; Jasik, P.; Młynarz, P.; Samoć, M.; Matczyszyn, K. Linear and Nonlinear Optical Properties of Azobenzene Derivatives Modified with an (Amino)Naphthalene Moiety. *J. Phys. Chem. B* **2022**, *126*, 6063−6073.

(24) Piovesan, E.; De Boni, L.; Ishow, E.; Mendonça, C. R. Two-Photon Absorption Properties of a Novel Class of Triarylamine Compounds. *Chem. Phys. Lett.* **2010**, *498*, 277−280.

(25) Gascón-Moya, M.; Pejoan, A.; Izquierdo-Serra, M.; Pittolo, S.; Cabré, G.; Hernando, J.; Alibés, R.; Gorostiza, P.; Busqué, F. An Optimized Glutamate Receptor Photoswitch with Sensitized Azobenzene Isomerization. *J. Org. Chem.* **2015**, *80*, 9915−9925.

(26) Chen, X.; Shi, X.; Yang, F.; Zhang, X.; Dai, R.; Jia, Y.; Yan, N.; Li, S.; Wang, Z.; Liang, Z. Physical Mechanism of One-Photon Absorption, Two-Photon Absorption, and Electron Circular Dichroism of 1,3,5 Triazine Derivatives Based on Molecular Planarity. *Molecules* **2023**, *28*, No. 4700.

(27) Skentzos, G.; Pramatioti, E.; Zink-Lorre, N.; Gutierrez-Vilchez, A. M.; Nikoli, E.; Canton-Vitoria, R.; Avramopoulos, A.; Tagmatarchis, N.; Fernandez-Lazaro, F.; Couris, S.Functionalization Tuning of the Nonlinear Optical Response of Perylene Diimide Derivatives *Mater. Adv.* 2026 DOI: 10.1039/D5MA01344E.

(28) Huang, G. Bin.; Shen, L.; Liu, J.; Zhou, W. F.; Traskovskis, K.; Song, Y. L.; Jiang, W.; Wang, Z. H.; Ren, X. K. Synthesis, Self-Assembly and Nonlinear Optical Activity of Selenium-Annulated Perylene Diimide. *Chem. Commun.* **2020**, *56*, 3123−3126.

(29) Gao, T.; Zhou, W. F.; Zhao, Y.; Shen, L.; Chang, W. Y.; Musendo, R. K.; Chen, E. Q.; Song, Y. L.; Ren, X. K. Polyhedral Oligosilsesquioxane Tethered Perylene Diimide for Application in Optical Limiting and Rapid Detection of Fluoride Ions. *Chem. Commun.* **2019**, *55*, 3012−3014.

(30) Szukalska, A.; Szkaradek, K.; Krupka, O.; Hudhomme, P.; Sahraoui, B.; Szukalski, A. Perylenediimide Polymers: Evaluating Third Harmonic Generation Responses for NLO Applications and Lasing Performance. *Adv. Opt. Mater.* **2025**, *13*, No. e02292.

(31) Yang, Y.; Wang, Y.; Xie, Y.; Xiong, T.; Yuan, Z.; Zhang, Y.; Qian, S.; Xiao, Y. Fused Perylenebisimide-Carbazole: New Ladder Chromophores with Enhanced Third-Order Nonlinear Optical Activities. *Chem. Commun.* **2011**, *47*, 10749−10751.

(32) Oliveira, S. L.; Corrêa, D. S.; Misoguti, L.; Constantino, C. J. L.; Aroca, R. F.; Zilio, S. C.; Mendonça, C. R. Perylene Derivatives with Large Two-Photon-Absorption Cross-Sections for Application in Optical Limiting and Upconversion Lasing. *Adv. Mater.* **2005**, *17*, 1890−1893.

(33) Sideri, I. K.; Jang, Y.; Garcés-Garcés, J.; Sastre-Santos, Á.; Canton-Vitoria, R.; Kitaura, R.; Fernández-Lázaro, F.; D'Souza, F.; Tagmatarchis, N. Unveiling the Photoinduced Electron-Donating Character of MoS$_2$ in Covalently Linked Hybrids Featuring Perylenediimide. *Angew. Chem., Int. Ed.* **2021**, *60*, 9120−9126.

(34) Yan, P.; Holman, M. W.; Robustelli, P.; Chowdhury, A.; Ishak, F. I.; Adams, D. M. Molecular Switch Based on a Biologically Important Redox Reaction. *J. Phys. Chem. B* **2005**, *109*, 130−137.

(35) Barrejón, M.; Pla, S.; Berlanga, I.; Gómez-Escalonilla, M. J.; Martín-Gomis, L.; Fierro, J. L. G.; Zhang, M.; Yudasaka, M.; Iijima, S.; Gobeze, H. B.; D'Souza, F.; Sastre-Santos, Á.; Langa, F. Covalent Decoration onto the Outer Walls of Double Walled Carbon Nanotubes with Perylenediimides. *J. Mater. Chem. C* **2015**, *3*, 4960−4969.

(36) Langhals, H.; Kirner, S. Novel Fluorescent Dyes by the Extension of the Core of Perylenetetracarboxylic Bisimides. *Eur. J. Org. Chem.* **2000**, *2000*, 365−380.

(37) Pagona, G.; Bittencourt, C.; Arenal, R.; Tagmatarchis, N. Exfoliated Semiconducting Pure 2H-MoS$_2$ and 2H-WS$_2$ Assisted by Chlorosulfonic Acid. *Chem. Commun.* **2015**, *51*, 12950−12953.

(38) Canton-Vitoria, R.; Sayed-Ahmad-Baraza, Y.; Pelaez-Fernandez, M.; Arenal, R.; Bittencourt, C.; Ewels, C. P.; Tagmatarchis, N. Functionalization of MoS$_2$ with 1,2-Dithiolanes: Toward Donor-Acceptor Nanohybrids for Energy Conversion. *npj 2D Mater. Appl.* **2017**, *1*, No. 13.

(39) Gan, Z. X.; Liu, L. Z.; Wu, H. Y.; Hao, Y. L.; Shan, Y.; Wu, X. L.; Chu, P. K. Quantum Confinement Effects across Two-Dimensional Planes in MoS$_2$ Quantum Dots. *Appl. Phys. Lett.* **2015**, *106*, No. 233113.

(40) Coehoorn, R.; Haas, C.; De Groot, R. A. Electronic Structure of MoSe$_2$, MoS$_2$, and WSe$_2$. II. The Nature of the Optical Band Gaps. *Phys. Rev. B* **1987**, *35*, No. 6203.

(41) Zhao, W.; Ghorannevis, Z.; Chu, L.; Toh, M.; Kloc, C.; Tan, P. H.; Eda, G. Evolution of Electronic Structure in Atomically Thin Sheets of WS$_2$ and WSe$_2$. *ACS Nano* **2013**, *7*, 791−797.

(42) Ford, W. E. Photochemistry of 3,4,9,10-Perylenetetracarboxylic Dianhydride Dyes: Visible Absorption and Fluorescence of the Di(Glycyl)Imide Derivative Monomer and Dimer in Basic Aqueous Solutions. *J. Photochem.* **1987**, *37*, 189−204.

(43) Gan, S.; Zhong, L.; Engelbrekt, C.; Zhang, J.; Han, D.; Ulstrup, J.; Chi, Q.; Niu, L. Graphene Controlled H- and J-Stacking of Perylene Dyes into Highly Stable Supramolecular Nanostructures for Enhanced Photocurrent Generation. *Nanoscale* **2014**, *6*, 10516−10523.

(44) Bonde, J.; Moses, P. G.; Jaramillo, T. F.; Nørskov, J. K.; Chorkendorff, I. Hydrogen Evolution on Nano-Particulate Transition Metal Sulfides. *Faraday Discuss.* **2009**, *140*, 219−231.

(45) Rowley-Neale, S. J.; Brownson, D. A. C.; Smith, G. C.; Sawtell, D. A. G.; Kelly, P. J.; Banks, C. E. 2D Nanosheet Molybdenum Disulphide (MoS$_2$) Modified Electrodes Explored towards the Hydrogen Evolution Reaction. *Nanoscale* **2015**, *7*, 18152−18168.

(46) Canton-Vitoria, R.; Matsunaga, Y.; Zhang, S.; Xue, M.; Osada, M.; Kitaura, R. Covalent Functionalization of Transition Metal Dichalcogenides with Perylene for Light Harvesting Devices. *Nanoscale* **2025**, *17*, 8084−8100.

(47) Woodward, R. I.; Kelleher, E. J. R. 2D Saturable Absorbers for Fibre Lasers. *Appl. Sci.* **2015**, *5*, 1440−1456.

(48) Chen, B.; Zhang, X.; Wu, K.; Wang, H.; Wang, J.; Chen, J. Q-Switched Fiber Laser Based on Transition Metal Dichalcogenides MoS$_2$, MoSe$_2$, WS$_2$, and WSe$_2$. *Opt. Express* **2015**, *23*, 26723−26737.

(49) Wang, S.; Yu, H.; Zhang, H.; Wang, A.; Zhao, M.; Chen, Y.; Mei, L.; Wang, J. Broadband Few-Layer MoS2 Saturable Absorbers. *Adv. Mater.* **2014**, *26*, 3538−3544.

(50) Wei, Z.; Guan, Z.; Shan, N.; Li, H.; Fang, Y.; Zhao, Y.; Fu, L.; Huang, Z.; Humphrey, M. G.; Zhang, C. Porphyrin Covalently Functionalized MoS$_2$ Nanosheets: "Click" Synthesis and Tunable Nonlinear Absorption. *J. Alloys Compd.* **2023**, *934*, No. 167902.

(51) Wang, Y.; Guo, Z.; You, J.; Zhang, Z.; Zheng, X.; Cheng, X. Ultrafast Nonlinear Optical Excitation Behaviors of Mono- and Few-Layer Two Dimensional MoS$_2$. *Photonic Sens.* **2019**, *9*, 1−10.

(52) Stavrou, M.; Chazapis, N.; Georgakilas, V.; Couris, S. 2D Non-van Der Waals Nanoplatelets of Hematene and Magnetene: Nonlinear Optical Response and Optical Limiting Performance from UV to NIR. *Chem. - Eur. J.* **2023**, *29*, No. e202301959.

(53) Diao, M.; Li, H.; Hou, R.; Liang, Y.; Wang, J.; Luo, Z.; Huang, Z.; Zhang, C. Vertical Heterostructure of SnS-MoS_2 Synthesized by Sulfur-Preloaded Chemical Vapor Deposition. *ACS Appl. Mater. Interfaces* **2020**, *12*, 7423−7431.

(54) Canton-Vitoria, R.; Gobeze, H. B.; Blas-Ferrando, V. M.; Ortiz, J.; Jang, Y.; Fernández-Lázaro, F.; Sastre-Santos, Á.; Nakanishi, Y.; Shinohara, H.; D'Souza, F.; Tagmatarchis, N. Excited-State Charge Transfer in Covalently Functionalized MoS_2 with a Zinc Phthalocyanine Donor−Acceptor Hybrid. *Angew. Chem., Int. Ed.* **2019**, *58*, 5712−5717.

(55) Cheng, H.; Dong, N.; Bai, T.; Song, Y.; Wang, J.; Qin, Y.; Zhang, B.; Chen, Y. Covalent Modification of MoS_2 with Poly(N-vinylcarbazole) for Solid-State Broadband Optical Limiters. *Chem. - Eur. J.* **2016**, *22*, 4500−4507.

(56) Shi, M.; Dong, N.; He, N.; Wan, Y.; Cheng, H.; Han, M.; Wang, J.; Chen, Y. MoS_2 Nanosheets Covalently Functionalized with Polyacrylonitrile: Synthesis and Broadband Laser Protection Performance. *J. Mater. Chem. C* **2017**, *5*, 11920−11926.

(57) Gan, F.; Dong, N.; Liu, Z.; Jia, H.; Wang, J.; Chen, Y. Organic Small Molecule Covalently Functionalized Molybdenum Disulfide Hybrid Material for Optical Limiting. *Bull. Chem. Soc. Jpn.* **2020**, *93*, 26−31.

(58) Li, W.; He, C.; Dong, Y.; Song, W.; Zu, Y. Zinc Phthalocyanine Carrying Sulfenyl and Sulfydryl Functionalized Sulfur Vacancies MoS_2 for Enhancement of the Third Order Nonlinear Optical Property. *Dyes Pigm.* **2022**, *198*, No. 109986.

(59) Rafi, R.; Sahni, A.; Abith, M.; Sabari Girisunb, T. C.; Sujatha, A. Fusing Organic and Inorganic Materials: Exploring Enhanced Optical Limiting in a Carmine−MoS_2 Hybrid. *Nanoscale* **2026**, *18*, 2215−2227 in press. DOI: 10.1039/d5nr03404c.

(60) Sheik-Bahae, M.; Said, A. A.; Wei, T.-H.; Hagan, D. J.; Van Stryland, E. W. Sensitive Measurement of Optical Nonlinearities Using a Single Beam. *IEEE J. Quantum Electron.* **1990**, *26*, 760−769.